University of Twente

MASTER THESIS

Investigation of Infragravity Waves in a Two-dimensional Domain using a non-hydrostatic numerical model, SWASH

Author:

Nikolaos ALAVANTAS

Supervisor:

Dr. ir. Jan S. RIBBERINK

Dr.ir. Bas BORSJE

Ir. Matthijs BENIT

Dr. ir. Gerbrant Ph. van VLEDDER

A thesis submitted in fulfillment of the requirements

for the degree of Master of Science

in the

Civil Engineering and Management

In collaboration with:

ARCADIS
Infrastructure · Water · Environment · Buildings

April 2015

UNIVERSITEIT TWENTE.

Declaration of Authorship

I, Nikolaos ALAVANTAS, declare that this thesis titled, 'Investigation of Infragravity Waves in a Two-dimensional Domain using a non-hydrostatic numerical model, SWASH' and the work presented in it are my own. I confirm that:

- This work was done wholly or mainly while in candidature for a research degree at this University.

- Where any part of this thesis has previously been submitted for a degree or any other qualification at this University or any other institution, this has been clearly stated.

- Where I have consulted the published work of others, this is always clearly attributed.

- Where I have quoted from the work of others, the source is always given. With the exception of such quotations, this thesis is entirely my own work.

- I have acknowledged all main sources of help.

- Where the thesis is based on work done by myself jointly with others, I have made clear exactly what was done by others and what I have contributed myself.

Signed:
_____

Date:
_____

Aknowledgements

Abstract

Investigation of Infagravity Waves in a Two-Dimensional Domain

by Nikolaos Alavantas

Infragravity waves (IG) are generated due to the non-linear interactions between the short (in terms of length) waves. IG waves propagate bounded to the short wave groups and they are released when fluctuations to the short wave energy occur. Aim of this research is to determine the behavior of IG waves around and inside the two-dimensional domain of Barbers Point Harbour on the island of Oahu, Hawaii, USA. In order to achieve simulation of IG waves, an extensive investigation is taking place, aiming to propose the most accurate numerical wave model for the particular case. The conclusion is that an efficient simulation of the harbour domain needs the usage of a phase-resolving and non-linear wave model, SWASH. SWASH showed consistency for the IG wave calculation (inside the basin of Barbers Point harbour) and its predictive skill measured approximately 0.84. Finally a further analysis is taking place, in order to decompose the IG signal. Aim is to separate the IG waves to free and bounded by using bispectral analysis and the separation method proposed by Sheremet et al. [2002]. The results are presented for the area outside the harbour. IG waves seem to be generated $500m$ seawards of the inlet. Additionally, the shore is identified as partially reflective boundary, even for the IG waves ($R_{IG}^2 = 0.6$). Finally, the behavior of the IG waves are affected by the entrance channel. IG waves (as long waves) are strongly refracted by the channel and continue to propagate inside the basin, when the short waves follow another path, leading to the adjacent shores.

Keywords: infragravity waves, modeling, SWASH, bispectral analysis, free IG waves, bound IG waves

Phase: fraction of wave cycle which has elapsed relative to the origin.

Turbulent energy: the mean kinetic energy per unit mass associated with eddies in turbulent flow.

Phase speed: the rate at which the phase of the wave propagates in space.

Shoaling: the effect by which surface waves entering shallower water increase in wave height. Wave speed and length decrease in shallow water, therefore the wave energy increases, so the wave height increases.

Refraction: is the change in direction of a wave due to a change in topography. Part of the wave is in shallower water and as a result is moving slower compared to the part in deeper water. So, the wave tends to bend when the depth under the crest varies.

Diffraction: is the change in direction of a wave due to an surface-piercing obstacle. Waves turn into the region behind the obstacle and carry wave energy and the wave crest into the "shadow zone". The tunning of the waves into the sheltered area is caused by the changes in the wave height, in the same wave.

Resonance: the tendency of a system to oscillate with greater amplitude at some frequencies than at others.

Vorticity: is a vector field that gives a microscopic measure of the fluid rotation at any point (the tendency of something to rotate).

Quadratic: is describing a second order relationship

Harmonics: is a component frequency of the wave signal.

Langarian velocity: the distance a water particle travels in one wave period, divided by that period.

Eulerian velocity: the short-wave-averaged velocity observed at a fixed point.

Dimensionless depth: Water depth, d, multiplied by the wave number, k.

Forchheimer dissipative terms: are developed for the macroscopic momentum and energy balance equations considering saturated thermoelastic porous media, and for the macroscopic momentum balance equations in the case of multiphase porous media.

Linear field: The area where the superposition principle can be applied. The net displacement of the medium at any point in space or time, is simply the sum of the individual (sine and cosine) wave displacements. In most of the cases, linear fields are located in deep or shallow waters.

Cos-spectrum: The cross-correlation between two time series as a function of frequency primar short wave frequency components

Primar frequency components: Frequency components where most of the energy is concentrated

Contents

List of Figures

List of Tables

Abbreviations

IG   **I**nfra**G**ravity

SWASH   **S**imulating **WA**aves till **SH**ore

XBeach e**X**tream **Beach** behaviour

FFT   **F**ast **F**ourier **T**ransformation

RANS   **R**eynolds **A**veraged **N**avier **S**toke equations

NSWE   **N**on-linear **S**hallow **W**ater **E**quations

CDIP   **C**oastal **D**ata **I**nformation **P**rogram

To my parents, Ourania and Konstantinos, for their endless love, support and encouragement...

Chapter 1

Introduction

1.1 Background

When wind blows over a fluid area (i.e. ocean) tends to formulate wind waves. Wind-waves could be classified as gravity waves (Figure 1.1), whose size varies between millimeters to dozens of meters [Munk, 1950] and they propagate shore-wards until they reach the shore. Furthermore, when wind events cease to exist, the wind-wave could be classified as swell. Swells are generated in a different (from where they are observed) place and they are not affected by the wind.
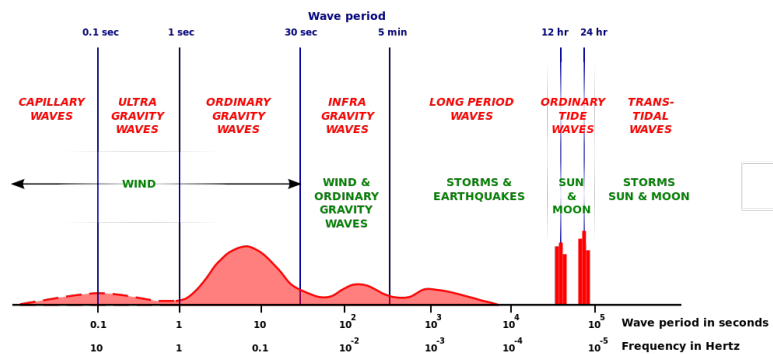
FIGURE 1.1: Energy spectrum for different types of waves[Munk, 1950].

High-frequency swell and wind waves generate, by non-linear interactions, bound infragravity waves (IG) [Longuet-Higgins and Stewart, 1962, Herbers and Burton, 1997] (Figure 1.2). These interactions can transfer a part of the short period waves energy into sub-harmonics. IG waves are traveling bounded with the short wave group, but in the opposite phase. Their periods are relatively long (periods between 20 and 200 s). They can occur offshore in the deep ocean [Webb et al., 1991], but they become larger and therefore more significant and stronger, closer to the shore [Guza and Thornton, 1985]. When swells and wind waves approach the coastline, they reach a critical level and a

large amount of their energy can be transformed to turbulent energy, due to breaking. During this energy dissipation, in shallow waters, IG waves are released. The bound IG wave transforms to free IG wave and partially is reflected by the shore. These free long waves have large wavelengths and phase speeds, and they follow the linear, surface gravity, wave dispersion. An insight to the IG waves will be given in Chapter 2. Generation, propagation and release of bound IG waves will be described.
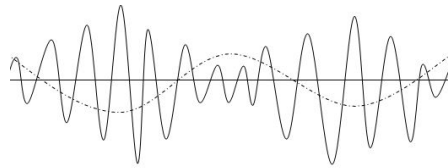
FIGURE 1.2: Short waves (solid line) travel in groups, and together they induce an infragravity wave (dashed line).

1.2 Motivation

IG waves and especially free IGs are highly interesting from an engineering perspective due to their impact in the coastal zone. IG waves can induce resonance [Chen et al., 2004a] or excessive vessel motions [Van Der Molen et al., 2006] inside the harbour basin. Furthermore, IG waves can cause suspended sediment transportation, especially under storm conditions [Beach and Sternberg, 1988]. In the case of ports, sediment transportation can cause down-drift erosion, scour at the base of breakwaters, silting- up of basins requiring repeated dredging, increased agitation due to the reflected waves or change of harbour opening characteristics [Leys and Mulligan, 2011]. So, prediction of IG wave propagation is very important from an engineering point of view.

Nowadays, many studies investigated the generation of IG waves and identified the release of bound IG waves , close to the shore, under high variation to the energy of short wave group. Most of them took under consideration an "one dimensional case" in order to quantify the effect of short wave's breaking to the transformation of IG waves (i.e. Buckley et al. [2014], Nwogu and Demirbilek [2010]). However, only a minority of them investigated IG waves in a "two dimensional domain", where evolution of IG wave could occur because of other phenomena, like diffraction and refraction. Therefore, there is a lack of knowledge about "two dimensional" IG wave behavior and modeling. In order to contribute to bridging the gap, a complex harbour case is chosen to be simulated (Chapter 4).

Additionally, wave simulation numerical tools (Chapter 3) still need validation. There is a lack of research about the performance of wave models in complex harbour domains

and their accuracy to predict the transformation and propagation of IG waves due to refraction, diffraction and partial reflection.

From a scientific point of view, the above mentioned uncertainties, were the reason that motivated me to proceed to that research.

1.3   Research question

Due to the complexity of the processes taking place in the progression of IG waves in the offshore but mostly in the near-shore area, there are still uncertainties in the propagation and transformation of bound IG waves and in the behavior of free IG waves. Numerical models tend to give inaccurate simulations of IG wave's evolution, mostly on the shore or shelf area. More specifically, some of the wave numerical models (i.e. SWASH Zijlema et al. [2011]) tend to underestimate shoreline reflection and as a result under-predict the magnitude of free IG waves throughout the domain [Buckley et al., 2014] whereas other models (i.e. XBeach [Roelvink et al., 2009]) underestimate dissipation and over-predict the height of IG wave, especially over steep slopes [Buckley et al., 2014]. The number of these uncertainties are increasing when the domain of investigation becomes two dimensional because of complex phenomena like diffraction, refraction, reflection and the existence of edge waves (Chapter 2.3).

Scope of this study is to provide insight in the propagation of bound IG waves and focus on the generation and evolution of free IG waves by using a wave numerical tool for near-shore areas. Emphasis will be given on their simulation and their effects in harbours. Leading to the primary research question in this thesis project:

"Which are the generation mechanisms of infragravity waves, how do they propagate through the domain and how the processes can be modeled in a two-dimensional case ?"

1.4   Objectives

The main objective of this thesis is to obtain insight in the generation, evolution, energy dissipation and separation of IG waves in two categories, the bound and the free part. Furthermore, this knowledge will be used to simulate IG wave propagation and effects, in a harbour case.

To answer the research question and fulfill the major objective a number of secondary questions are formulated:

1. For Chapter 2, Infragravity waves

   (a) How are bound IG waves generated and under which typical conditions?

   (b) How are free IG waves generated, how could they be classified according to their origin and how important is each classification for harbour cases?

   (c) Which are the dissipation mechanisms of IG waves?

2. For Chapter 3, Numerical modeling

   (a) Which are the most widely used wave numerical models and how they could be characterized?

   (b) According to literature, which are the limitations of the numerical tools in a two-dimensional IG wave simulation ?

   (c) Are these IG wave models capable to directly provide characteristic of IG waves (i.e. significant height), or is an additional method required for output analysis?

   (d) According to the obtained knowledge, which model(s) has to be used in order to obtain accuracy and reasonable computational time (in Barbers Point harbour case)?

3. For Chapter 4 and Chapter 5, Barbers Point Harbour (two-dimensional) case

   (a) Determine the simulation time in order to achieve statistically accurate calculation for the IG waves

   (b) How large and what resolution in space and time should the simulated domain have, and what will be the effects to the accuracy and duration of simulation?

   (c) What boundary conditions are required?

   (d) What are the reflection characteristics of boundary (shore) layers?

   (e) How sensitive is the numerical wave model for the unknown input parameters (i.e. grid resolution, breaking parameters,sponge layers) ?

   (f) How accurate are the calculations of the IG waves compared to field measurements (model validation)?

4. For Chapter 6, IG wave decomposition

   (a) Is bispectral analysis (as a decomposition method) applicable inside the basin?

   (b) How can we decompose the incoming from the out-coming IG wave?

   (c) How do short waves transmit energy to IG waves and dependable is this transmission on the depth (intermediate depths, surf-zone) ?

   (d) How the IG wave behave when it is reflected (fully or not reflected)?

These are the main research question which are addressed in this thesis. A summary of answers is given in Chapter 7.

1.5 Thesis outline

The initial step in the present study is to identify the fundamental characteristics of IG waves. Insight in the generation, propagation, dissipation (in the offshore and near-shore area) and reflection of IG waves is obtained in Chapter 2. Simultaneously, discretization of different types of IG waves depending on their relevancy to harbour problems is presented. Then, Chapter 3 presents the available numerical wave models, an extensive comparison of them, and concludes to that one which performs more accurate in the case of Barbers Point harbour. Both of these chapters are part of the literature review.

Chapter 4 presents the case which is selected to be investigated. IG wave behavior is investigated for the case of Barbers Point harbour in Oahu, Hawaii, USA. Additionally, the bathymetry and the offshore wave conditions are shown. Finally, there is a first try to identify the correlation of the IG with the short waves, in order to determine, qualitatively, the boundedness between IG-short waves.

However, there are several parameters (i.e sponge layers) which are not available a priori and there are important to achieve an accurate simulation. A sensitivity analysis (Chapter 5) for these parameters is carried out, in order to define them. Finally, the input data are determined and the simulated IG wave characteristics are compared with the field measurements (model validation).

Finally, in Chapter 6, IG wave is analyzed by using bispectral analysis. The aim is to decompose the IG wave to the free and bounded component. The last step is a further separation of the IG wave to the incoming and outgoing part by using the method of Sheremet et al. [2002].

Conclusions and recommendations for future research are given in Chapter 7.

Chapter 2

Infragravity waves

As explained in Chapter 1, infragravity waves are surface gravity waves with long periods (0.005- 0.05 Hz) and their energy contribution is presented in Figure 1.1. Firstly, they observed as surf-beat and determined by Longuet-Higgins and Stewart [1962]. Due to non-linear interactions between group of high waves, bounded (to this group) IG waves are generated and their energy increases shore-wards. After high variabilities (spatial and temporal) in the energy of the group (i.e. breaking, reflection), they are released in the form of freely propagating waves. Recent studies have shown that they are important (high impact) to coastal-zone areas, such as oscillations in harbours, sediment transport and excessive motions to the moored vessels (Chapter 1.2).

In this section, an extensive presentation of IG wave's generation and spatial behavior, and formation differences of free IG waves are given. The study is harbour engineering oriented and as a result there will be a presentation of significance of each IG wave formation (bound, free, leaky and edge IG wave) for the design of ports.

2.1 Generation and propagation

In offshore regions wind waves are generated and they tend to travel in groups. It is observed that the water level is depressed under such a group of waves. This depression can be explained by using the radiation stress concept of Longuet-Higgins and Stewart [1962].

According to Longuet-Higgins and Stewart [1962], a group of waves outside the boundary layers contains a second-order vorticity, which is associated with a steady second-order current (bound IG wave) and does not affect the distribution of pressure. After the identification of IG waves, Longuet-Higgins and Stewart [1962] provided a second-order

solution for the surface elevation ζ and the velocity potential ϕ by expanding the Stokes method of approximation:

$$\zeta = \zeta^{(1)} + \zeta^{(2)} + ... \tag{2.1}$$

$$\phi = \phi^{(1)} + \phi^{(2)} + ... \tag{2.2}$$

where $\zeta^{(1)}$ and $\phi^{(1)}$ satisfy the linearised equations and boundary conditions and $\zeta^{(1)}+\zeta^{(2)}$, $\phi^{(1)}+\phi^{(2)}$ satisfy the equations as far as the quadratic terms and so on. For simplicity reasons, if it is assumed that incident wave consists of two unidirectional harmonics (bichromatic), the solution follows up for Eqs.(2.3 and 2.4).

$$\zeta = \zeta_1 + \zeta_2 + \zeta_{1,2} \tag{2.3}$$

$$\phi = \phi_1 + \phi_2 + \phi_{1,2} \tag{2.4}$$

where ζ_1, ζ_2, ϕ_1 and ϕ_2 are relevant with the primary short waves and $\zeta_{1,2}$ and $\phi_{1,2}$ are describing the second-order solution which is a combination of a sub (i.e. bound IG wave) and a super harmonic wave, which are forced by the difference and sum interactions, respectively [Rijnsdorp et al., 2012]. Figure 2.1 shows the energy transmission to sub and super harmonics, as the waves propagate, for a narrow peaked spectrum [Michallet et al., 2014].
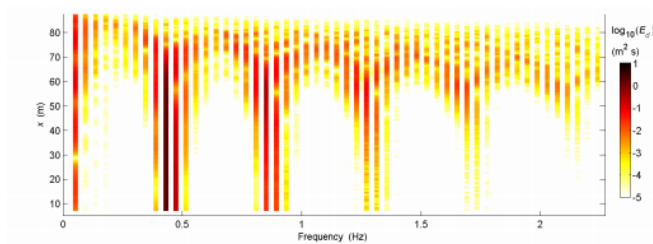
FIGURE 2.1: Spectral evolution as a friction of the cross-shore position (x) and the frequency (f) [Michallet et al., 2014]

Bound IG, as predicted from the second-order Stokes theory, is quadratic related to the energy of shorter energies (Figure 2.2) and that relation confirmed by Herbers et al. [1995], who investigated this relation in high depths, where bound IG waves are generated.

Recent studies suggested that the propagation of bound IG waves depends on its frequency [Battjes et al., 2004]. When its frequency is relatively high, IG wave behaves as Longuet-Higgins and Stewart [1962] described. On the other hand, when frequency decreases, IG wave can be described more accurately by Green's law [Synolakis, 1991]. As Battjes et al. [2004] observed this is caused because of the (slightly) larger phase differences of the lower frequencies, which allows more energy to be transformed from the
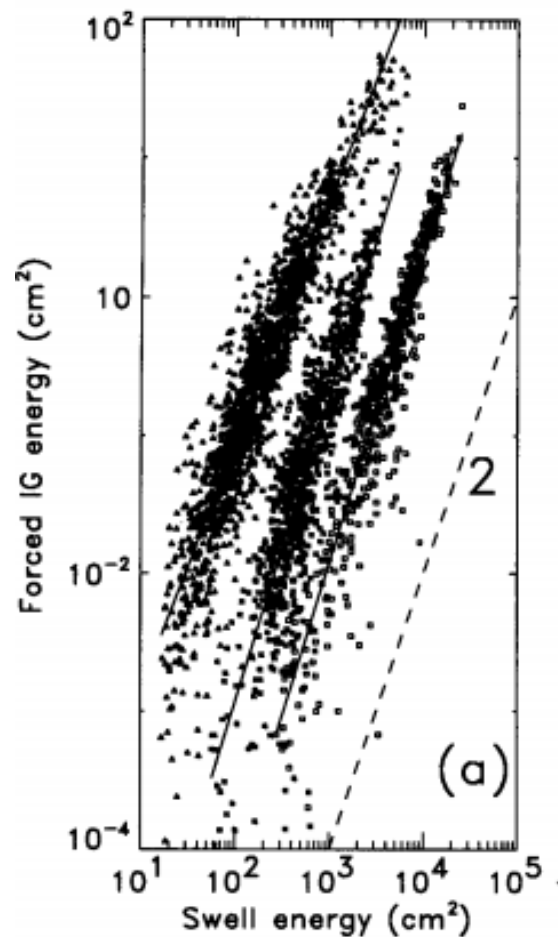
FIGURE 2.2: Bound IG wave energy compared with swell energy for different locations. Energy decreases as depth increases [Herbers et al., 1995].

group of short waves. Cross-shore energy evolution per wave frequency band is shown in Figure 2.3.

Finally, bound IG waves can cause direct impact to the harbours only during storms and due to swells [Nakaza and Hino, 1991]. Additionally, negative effects on the construction depend on the width of the entrance and how much bound IG wave energy will penetrate to the harbour. In most of the cases, harbours are well protected from short waves and their bounded long waves but it is hard to prevent the existence of released long waves (Chapter 2.2), which are propagating freely.

2.2   Incident free long waves

Generally, generation mechanism of free IG can be separated in two categories:
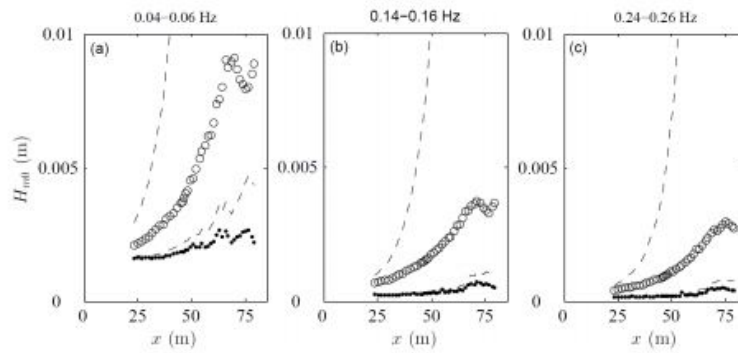
FIGURE 2.3: H_{m0} values of incoming (triangles) and outgoing (dots) IG waves for different frequency bands. Lower dashed curve: Green ($H \sim h^{1/4}$), fitted to outgoing wave heights in the zone offshore from x = 20 m; upper dashed curve: Longuet-Higgins and Stewart [1962] asymptote ($H \sim h^{5/2}$), initiated with wave height at x = 8 m.[Battjes et al., 2004]

- Bound IG waves generated by non-linear interactions are released as free when high decrease in the short wave energy is occurred [Longuet-Higgins and Stewart, 1962].

- Time-varying break point of short wave groups [Symonds et al., 1982].

Firstly, Longuet-Higgins and Stewart [1962] investigated the generation of IG waves and argued that they are propagating bounded with short wave groups. In the surf zone (or wherever there are high fluctuations to the short wave energy) the wave group dissipates and the IG wave is released. On the other hand Symonds et al. [1982] suggested that due to the radiation stress strong gradients in the surf zone, a set up at the shore line is caused. The conclusion is that the break point varies through time and this set-up (which varies with the time wave group scale) can be recognized as a free IG wave propagating shore-wards (in phase) and seawards (out of phase). According to Battjes et al. [2004] and Dong et al. [2009], the second mechanism is dominant at steep slopes and the first to the milder.

In contrast with the more quadratic relation of swell/storm and bound IG wave, free IG waves seem to be more linearly proportional to the short waves (Figure 2.4). Herbers et al. [1995] determined that breaking is the most important generation procedure for free IG waves. However, Zhou and Liu [1987] proved theoretically, that bound IG waves could be released as free due to the diffraction, close to the basin's inlet. Still, there is no research (especially on the field) which agrees with that release mechanism. The investigation of IG release is done by using bispectral analysis and more details about this method are presented in Chapter 3.2.
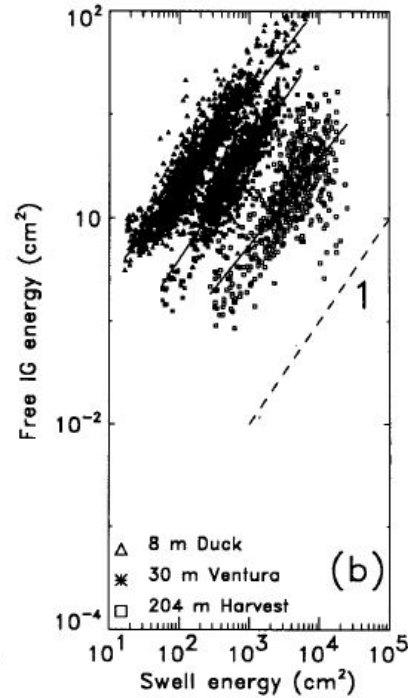
FIGURE 2.4: Linear relation of free IG waves measured in different locations [Herbers et al., 1995].

Nowadays, modern harbour designers tend to locate the entrance in a water depth (at least) twice the height of a design storm wave, in order to prevent negative impacts, on vessels, by wave breaking [McBride et al., 1996]. This channel depth is depending mainly on draught and wave length. Aim of harbour engineers is to avoid wave breaking phenomenon inside the channel or in the basin. However, this does not mean that harbours are protected by free long waves generated by breaking. McComb et al. [2009] proved that high energies from long waves that can induce resonance originated from free IG waves. These free IG waves are generated by breaking in the adjacent reef area and refracted, due to the entrance channel, inside the basin (Figure 2.5).

2.3   Reflected infragravity waves

IG waves are considered fully reflected from the shore or partially by an obstacle (i.e. wall, breakwater) [Sheremet et al., 2002, Herbers et al., 1995, Battjes et al., 2004]. After their reflection IG waves can de-shoal to offshore regions (leaky wave) or remain trapped into the surfzone (edge wave). Decomposition of reflected waves is complex but it can be done by using the wave number spectrum [Holland and Holman, 1999] and it is presented Figure 2.6. According to Holland and Holman [1999], in the frequency band of IG waves (0.005-0.05 Hz), high absolute and low absolute wave numbers represent edge and leaky waves respectively.
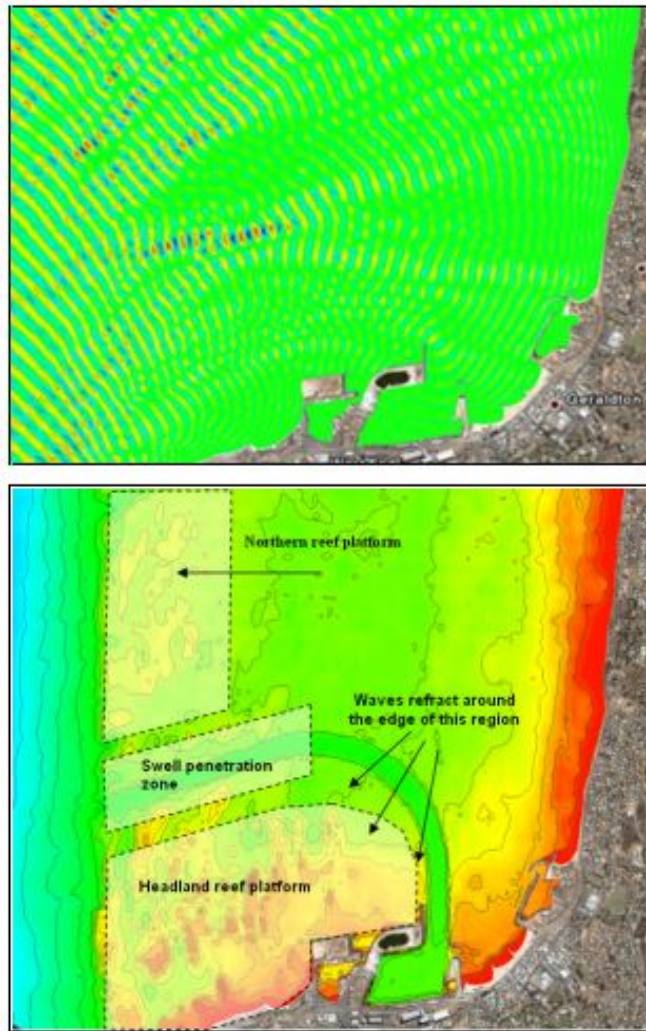
FIGURE 2.5: Upper plot shows the typical swell wave patterns, lower plot details about the topography and the areas where free IG waves refracted and penetrate to the basin [McComb et al., 2009].
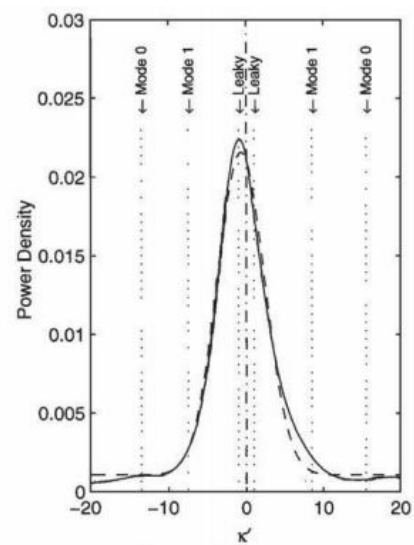
FIGURE 2.6: A typical separation of reflected IG waves according to their wave-number, presented by Holland and Holman [1999]

As explained leaky waves are freely seaward propagating IG waves (Figure 2.11, panel
(d), (e) and (f)). They are generated from an obstacle and they are important for
near-shore sediment transport and creation of standing waves close to beaches (surf or
swash zone). From a harbour engineering perspective, leaky waves are important for the
construction because they can induce oscillations to the moored vessels inside the basin
[Harkins and Briggs, 1994].

The lateral type of reflected IG wave is the edge wave (Figure 2.9). When the angle
of the incident wave is relatively high the free IG reflected wave can be trapped due
to refraction in the surf-zone (Figure 2.10). Firstly, edge waves identified by Stokes
who tried to determine their propagation speed. Finally, Ursell [1952] proved that edge
waves can be described by different modes and that the Stokes theory consist the lowest
of these modes. These modes represents the number of zero amplitude crossings, in
cross-shore direction (Figure 2.7).
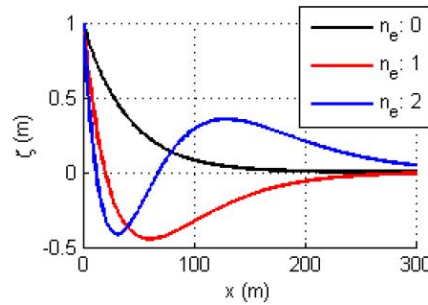
FIGURE 2.7: Three different edge wave modes (0,1 and 2) [Van Giffen, 2003]

In order to determine the incoming and outgoing (reflected) IG waves the method of
Sheremet et al. [2002] is proposed. The energy of the incoming and reflected waves are
calculated as:

$$E^{\pm}(f) = 0.25(Co_{\eta\eta}(f) + h/gCo_{uu}(f) \pm (2\sqrt{h/g})Co_{\eta u}(f) \tag{2.5}$$

and the corresponding IG energy flux is given by:

$$F^{\pm}(f) = E^{\pm}(f)\sqrt{gh} \tag{2.6}$$

where $Co_{\eta u}$ is the cospectrum between the surface elevation (η) and the velocity for
the mean direction (u). Furthermore, $Co_{\eta\eta}$ and Co_{uu} is the autospectra for the surface
elevation and the velocity, respectively, h is the depth and g is the gravitational acceler-
ation. Finally both energies (E) and fluxes (F) are calculated for the IG wave frequency
band (0.005-0.05 Hz). Reflection coefficient (R) is given by:

$$R^2 = F^-/F^+ \tag{2.7}$$

de Bakker et al. [2013] determined that the incoming fluxes grow until the breaking point and after that diminishes, when the outgoing flux remains relatively constant (Figure 2.8, upper panel). The reflection coefficient (Figure 2.8, bottom panel) slightly decreases close (from the offshore side) to the breaking point and after that becomes steady.
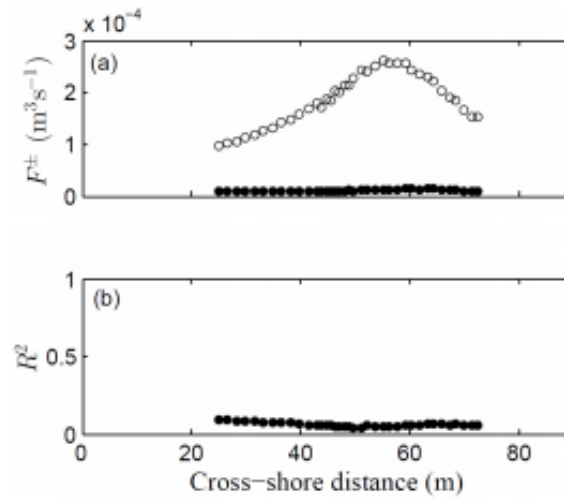
FIGURE 2.8: (a) Bulk incoming (circles) and outgoing (black dots) infragravity energy fluxes (F±) and (b) bulk reflection coefficients (R2) for the infragravity wave band [de Bakker et al., 2013].

From an engineering perspective, existence of edge waves can cause resonance to harbours and oscillations to vessels. Negative impact of edge waves proved theoretically by Bowers [1977] and practically by Ciriano et al. [2001] and Chen et al. [2004b]. The complex effects of edge waves are under investigation and it is difficult to propose proper solutions for this new type of resonance. Nowadays, harbour engineers are capable to counter the lowest (simplest) modes of these edge waves by redirecting the reflected IG waves. Breakwaters alongshore and inside the surfzone could redirect the edge waves outside of a harbour basin as Chen et al. [2004b] proposed.

2.4 Dissipation mechanisms

At low water depths and close to the shore, IG waves energy decreasing. This energy dissipation can be caused by several reasons and in this research the most significant of them, according to literature, are presented.
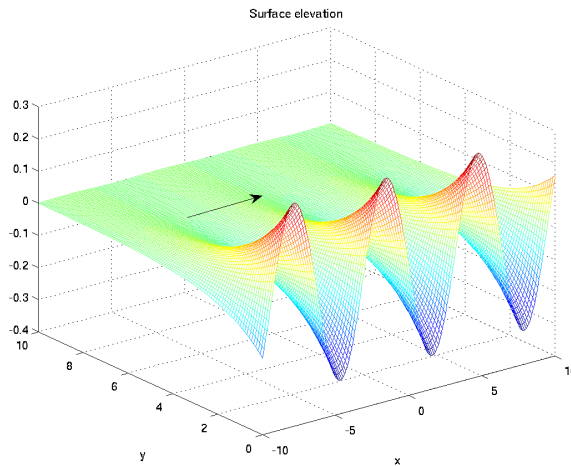
FIGURE 2.9: Propagation of a Stokes (zero mode) edge wave alongshore [Van Giffen, 2003] .
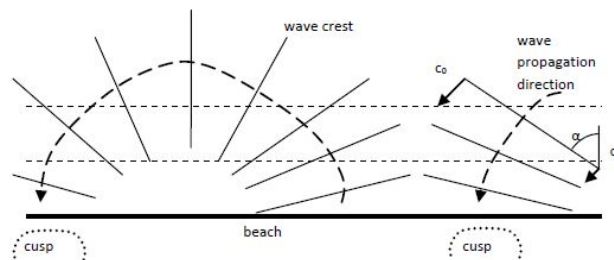
FIGURE 2.10: Generation of an edge wave due to de-shoaling and refraction [Van Giffen, 2003] .

At first, Thomson et al. [2006] determined that it is possible reflected IG waves transmit some of their energy to the short wave groups. This can occur inside the surf-zone before the breaking point. Eventually, this energy will be dissipated after the breaking of short waves. This mechanism can be interesting when engineers are trying to simulate the propagation of edge waves.

Additional, an other dissipation mechanism can be the breaking of IG wave as Van Dongeren et al. [2007] explained. Under extreme storm conditions, freely propagating IG wave can continue the shoaling process shore-wards and at a certain point, breaks (Figure 2.11, panel (b)).

The last mechanism is bottom friction. Henderson and Bowen [2002] proved that energy of IG wave can dissipate due to the bottom friction. However, more recent research by Henderson et al. [2006] determined that for small drag coefficients this mechanism can be neglected. Furthermore, Rijnsdorp et al. [2014] showed that the bottom friction has marginal effect on incoming IG waves. In case of mildly reflective, bottom friction has a significant influence on the evolution of outgoing IG waves.
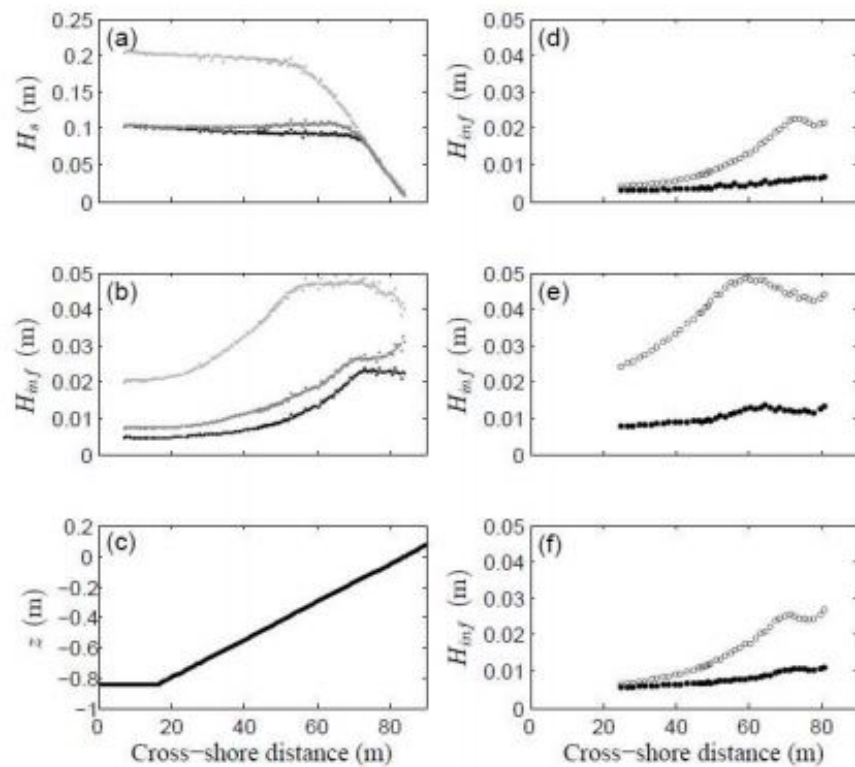
FIGURE 2.11: Significant wave height versus cross-shore distance x for (a) short waves H_s and (b) infragravity waves H_{inf} for different locations: A1 (black dots), A2 (light-grey dots) and A3 (dark-grey dots). (c) Bed profile. Furthermore, the significant incoming (circles) and outgoing (black dots) infragravity-wave heights calculated from separated signals (following Guza et al., 1984) are shown for (d) A1, (e) A2 and (f) A3 [de Bakker et al., 2013].

Chapter 3

Numerical modeling and IG analysis

Recently many numerical models developed in order to simulate wave transformation and morphological processes. Nowadays, two main classes of wave models are available:

- **Phase-averaged models**: operate in a frequency domain
- **Phase-resolving models**: operate in a time domain

Phase-averaged models are not capable to calculate surface elevation in an exact location, but they predict the average variance (or energy) of surface elevation . Results of a phase-averaged model correspond to integral spectral wave parameters (i.e. significant wave height) of the wave field. They are using the energy balance equation in order to describe the spectral evolution and they considered as "computational cheap". Due to these characteristics, they are suitable for simulating cases over long distances where the depth changes slowly [Monbaliu et al., 2000]. These models neglect or approximate wave transformation processes such as wave diffraction, reflection, and non-linear interactions, so they are not able to simulate accurately IG waves.

Phase-resolving models are able to calculate sea surface in time and space by using one of these three types of equations:

- Reynolds Averaged Navier Stoke equations (RANS)
- Boussinesq equations
- Non-linear shallow water equations (NSWE)

- Mild-Slope equations

Output of these models is a picture of sea surface elevation fields for each of the modelling time step which makes them computationally expensive. In contrast with phase-averaged models, they can simulate accurately phenomena like diffraction, refraction an reflection and calculate IG wave characteristics. Phase-resolving models are used in small domains where there are rapidly changes to the wave local properties (i.e harbours, close to breakwaters).

Compared to Boussinesq models (i.e. SURF-GN [Bonneton et al., 2011]), implementation of NSWE models is less complex, thereby they have improved robustness and it is easier to maintain them [Rijnsdorp et al., 2012]. Additionally, Boussinesq models are able to calculate both short and long waves, including all the relevant processes (i.e. refraction, diffraction, non-linearity) and the bulk dissipation associated with the wave breaking, but not the detailed breaking process itself [Rijnsdorp et al., 2014]. Nevertheless, Boussinesq models applied and validated for short wave motions, including breaking (i.e. Tonelli and Petti [2012], Tissier et al. [2012]), but only a minority of them extended to IG wave investigation [Madsen et al., 1997]. On the other hand, NSWE models have shown great potential to simulate wave propagation, including non-linear wave-dynamics [Rijnsdorp et al., 2014, Smit et al., 2013] and to calculate accurately IG-motions [Rijnsdorp et al., 2012, Ma et al., 2012]. Finally, NSWE can perform accurately and with the same computational effort as Boussinesq models. Finally, Boussinesq models are not accurate in deeper water due to the absence of vertical-layer discretization [Rijnsdorp et al., 2014].

Furthermore, RANS models (i.e COBRAS-UC [Lara et al., 2008]) need a lot of computational resources [Suzuki et al., 2012] especially when the case is two-dimensional. RANS models can not efficiently compute the free surface flow by considering the free surface as a single valued function (as NSWE models are able to do) and due to this characteristic are relatively computational "expensive" [Rijnsdorp et al., 2014]. Mild-slope models are limited and they can not take into account the phenomenon of reflection [Lee et al., 1998]. This feature of the mild-slope models make them unsuitable for harbour cases and steep-slopes.

NSWE models are relatively (computationally) cheap and applicable for harbour cases and steep slopes in intermediate and shallow depths. Additionally, the implementation of the non-hydrostatic term makes them capable to take into account weakly dispersive waves (i.e. IG waves). The most widely used non-hydrostatic NSWE models are the SWASH [Zijlema et al., 2011] and XBeach- non-hydrostatic Roelvink et al. [2009]. XBeach- non-hydrostatic and SWASH is based upon Stelling and Zijlema [2003].

In XBeach, vertically a compact scheme is used which allows an inclusion of the boundary condition of the dynamic pressure at the free surface. The dispersive waves can be modeled using a depth average flow model. The application of momentum conservative numerical schemes allows the accurate modelling of wave breaking without the need of a separate breaking model. However, because XBeach is a depth averaged model, only the single layer version was implemented. Due to the one-layer feature XBeach (like Boussinesq models) is inaccurate at large depths. A comparison of XBeach with SWASH is given in Figure 3.4, showing that XBeach tends to underestimate and overestimate IG waves at the breaking and surf-zone respectively, due to the low vertical resolution.

In this thesis, the open-source and widely used numerical model SWASH [Zijlema et al., 2011] is used in order to simulate accurately IG wave propagation and transformation (Chapter 3). SWASH is a phase-resolving NSWE model and it can run in a multi-layered mode with improved frequency dispersion properties. SWASH is considered capable to simulate IG waves [Buckley et al., 2014] and its fundamental characteristics will be presented in Chapter 3.1. Aim is to conclude to the advantages and the limitations of SWASH for a two-dimensional case .

3.1 SWASH

SWASH (Simulating WAves till SHore) is a non-hydrostatic, phase-resolving non-linear wave numerical model, developed by Zijlema et al. [2011]. It is a general-purpose numerical-tool for simulating hydrodynamic and transport phenomena in shallow water areas. Furthermore, simulations could be two or even three dimensional. Aim of this model is to provide an efficient and robust model which can applied in complex domains like harbours, rivers, estuaries and large-scale oceans.

3.1.1 Fundamental equations

Objective of this section is to present and give insight to SWASH governing equations. It should be mentioned that SWASH is capable to discretize the domain in vertical direction and simulate that as equidistant layers. In order to describe the free-surface, model solves the NSWE including the term of non-hydrostatic pressure (derived by Navier-Stokes equations) for an incompressible flow.

$$\frac{\partial \zeta}{\partial t} + \frac{\partial hu}{\partial x} + \frac{\partial hv}{\partial y} = 0 \tag{3.1}$$

$$\frac{\partial u}{\partial t} + u\frac{\partial u}{\partial x} + v\frac{\partial u}{\partial y} + g\frac{\partial \zeta}{\partial x} + \frac{1}{h}\int_{-d}^{\zeta}\frac{\partial q}{\partial x}dz + c_f\frac{u\sqrt{u^2+v^2}}{h} = \frac{1}{h}(\frac{\partial h\tau_{xx}}{\partial x} + \frac{\partial h\tau_{xy}}{\partial y}) \tag{3.2}$$

$$\frac{\partial v}{\partial t} + u\frac{\partial v}{\partial x} + v\frac{\partial v}{\partial y} + g\frac{\partial \zeta}{\partial x} + \frac{1}{h}\int_{-d}^{\zeta}\frac{\partial q}{\partial x}dz + c_f\frac{v\sqrt{u^2+v^2}}{h} = \frac{1}{h}(\frac{\partial h\tau_{yx}}{\partial x} + \frac{\partial h\tau_{yy}}{\partial y}) \quad (3.3)$$

where x and y is the cartesian coordinates, t is the time, ζ is the surface elevation from the still water level, d is the still water depth, $h=\zeta+d$ is the total water depth, u and v the depth-averaged flow velocities, q the non-hydrostatic pressure, g the gravitational acceleration, c_f the bottom friction coefficient and $\tau_x x$, $\tau_x y$, $\tau_y x$ and $\tau_y y$ are the turbulent stress terms.

According to Stelling and Zijlema [2003] non-hydrostatic pressure q can be expressed as:

$$\int_{-d}^{\zeta}\frac{\partial q}{\partial x}dz = \frac{1}{2}h\frac{\partial q_b}{\partial x} + \frac{1}{2}q_b\frac{\partial(\zeta-d)}{\partial x} \quad (3.4)$$

where q_b is the non-hydrostatic pressure at the bottom. Combination of Keller-box method [Lam and Simpson, 1976] and momentum equations for the vertical velocities in z-direction at the free surface, w_s, and at the bed level, w_b, produce Eq 3.5 .

$$\frac{\partial w_s}{\partial t} = \frac{2q_b}{h} - \frac{\partial w_b}{\partial t} \quad (3.5)$$

Additionally, vertical velocity w_b, can be given from the kinematic condition:

$$w_b = -u\frac{\partial d}{\partial x} - v\frac{\partial d}{\partial y} \quad (3.6)$$

At the end, velocities can be expressed from the conservation of local mass as:

$$\frac{\partial u}{\partial x} + \frac{\partial v}{\partial y} + \frac{w_s-w_b}{h} = 0 \quad (3.7)$$

To conclude, SWASH model tends to solve the tree Eqs. 3.1, 3.2 and 3.3 in order to determine the values of three unknowns, flow velocities u and v and the surface elevation ζ, at each layer.

3.1.2 Boundary conditions

A simplified version of the domain is presented to the Figure 3.1 which shows the boundaries. Conditions, which are used in order to solve Eqs. 3.1, 3.2 and 3.3, are given for each boundary, separately. In general, boundary conditions for SWASH are layer averaged velocities and surface elevation series. These series can be imposed directly or estimated by the model from spectra or fourier parameters.
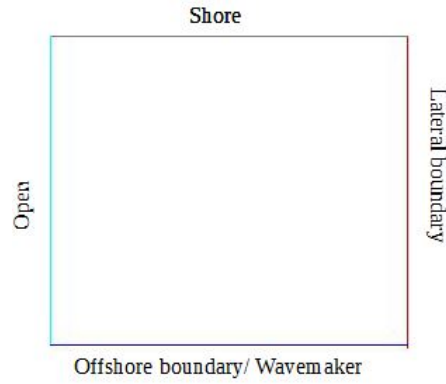
FIGURE 3.1: Simplification of the domain with the different types of the boundaries.

3.1.2.1 Offshore

An incident wave(s) can be imposed as uni or multi-directional. For regular waves, the parameters of height and period have to be specified. Alternatively, a surface time series can be implemented. On the other hand, when the waves are irregular user has to choose between the spectrum or a time series as input data. Shapes of spectrum can be either the usual (Jonswap, Pierson-Moskowitz), TMA (modified from the user) or given entirely form the user (1-D non-directional or 2D directional wave spectrum).

Additionally, a weakly reflective condition which allows outgoing waves and avoid the reflection of incoming is introduced [Blayo and Debreu, 2005]:

$$u_b = \pm\sqrt{\frac{g}{h}}(2\zeta_b - \zeta) \tag{3.8}$$

3.1.2.2 Shore

Generally, shore is assumed a moving shoreline in order to take into consideration wave run-up and inundations. In addition, obstacles like constructions and breakwaters are schematized by including their slopes and by means of porosity layers (rubble mound breakwaters). Constructions are highly reflectional and because of that the Sommerfeld's radiation condition (Eq. 3.9) is implemented, which allows reflective waves to cross the offshore boundary layer.

$$\frac{\partial u}{\partial t} + \sqrt{gh}\frac{\partial u}{\partial x} = 0 \tag{3.9}$$

3.1.2.3   Lateral boundary

A lateral boundary is implemented in order to be viable the calculation of Eqs. 3.1, 3.2 and 3.3 in the Open-Lateral (along-shore) boundary (Figure 3.1) direction. For simplicity, it is better to assume that as fully reflective. These assumption yields to locate gauges (location of interest) outside of the effected area from "lateral boundary"reflected waves.

3.1.3   Wave breaking

In Chapter 1 and in Chapter 2, it is identified that breaking phenomena have a major contribution to the IG wave release. The wave breaking structure is defined by using SWASH and the bore formation concept [Smit et al., 2013]. The initiation of a wave breaking process occurs when the fraction of the shallow water celerity is lower than the vertical speed of the free surface (Eq 3.10).

$$\frac{d\zeta}{dt} > a\sqrt{gh} \qquad (3.10)$$

where a is a parameter related to the surface slope and ζ is the surface elevation. By default, a is 0.6, which corresponds to the front steepness of 25°. The wave breaking zone continues until the local steepness reach the value β (by default 0.15) (Eq 3.11).

$$\frac{d\zeta}{dt} < \beta\sqrt{gh} \qquad (3.11)$$

3.2   Post data analysis and the decomposition of IG waves

The fist step of the post data analysis is the separation of short and IG waves. In order to achieve that a wave energy spectrum has to be constructed for each simulated location point. Energy spectrum visualize the magnitude of all the possible wave frequencies. In order to construct the wave energy spectrum FFT (Fast Fourier Transform) is considered as the most valuable, signal analysis, computational tool.

Aim of the FFT method is to efficiently compute the Fourier transform. For given time-series, Fourier transform decomposes the signal to the frequencies that it is considered. Result is infinite sine and cosine waves with frequencies that start form 0 and increase in integer multiples of a base frequency (1 divided by total length of the time signal). Fourier series are given by Eq 3.12

$$f(x) = a_0 + \sum_{n=1}^{\infty} a_n \cos nt + \sum_{n=1}^{\infty} b_n \sin nt \tag{3.12}$$

where t is the time and $f(t)$ is the time-series and the objective of the Fourier transformation is to determine the parameters a_n and b_n. Finally, short and IG waves are decomposed by knowing their frequency bands.

Continuing, an objective of this thesis is the separation of IG waves to free and bound. Decomposition of the IG waves is significant in order to analyze the IG waves and identify the generation mechanism of these IG waves. Several methods (Kostense [1984],Ma et al. [2011]) are proposed for separating IG waves. However, in this study, the rate of the bound to the released IG waves are investigated in terms of the bispectrum $B(f_1, f_2)$ [Hasselmann et al., 1963]. Bispectal analysis have been applied in several studies (Guza and Thornton [1985],Ruessink [1998],Sheremet et al. [2002]) showing consistency and efficiency when it is applied in intermediate and shallow waters. Unfortunately , separation by using bispectrum becomes incapable [Dong et al., 2010] to predict the separation of IG waves at locations affected by resonance (e.g inside a harbour basin). The bispectrum is given by Eq 3.13

$$B(f_1, f_2) = E(a_{f_1} a_{f_2} a_{f_1+f_2}) \tag{3.13}$$

where $E()$ is the expected value, a_{f_n} represents the complex Fourier coefficient (at the nth frequency) and the * is the complex conjugate. The statistical dependence among three different frequency components (f_1,f_2 and f_1+f_2) is computed by bispectrum. When the frequency components become independent (have random phases), bispectrum is nullified and the field can be considered as a linear superposition of wave components. However, in the case of IG waves non-linear interactions between primary and bound waves leads to $B(f_1, f_2)$ different than zero. Coupling of these waves (primary and bound) can be measured by the normalized magnitude of the bispectrum (or bicoherence), $b(f_1, f_2)$ (Eq 3.14) and the normalized bispectrum phase (or biphase), θ (Eq 3.15) given by Kim and Powers [1979]

$$b(f_1, f_2) = \frac{B(f_1, f_2)}{\sqrt{E(f_1)E(f_2)E(f_1 + f_2)}} \tag{3.14}$$

and

$$\theta(f_1, f_2) = tan^{-1}[Im(B(f_1, f_2))/Re(B(f_1, f_2))] \tag{3.15}$$

where Re is the real and Im the imaginary part and the value of b can be between between 0 and 1 (Kim and Powers [1979], Guza and Thornton [1985]). The real part, Re, describes the wave skewness, the imaginary part, Im, describes the symmetricity in a statistical sense and the biphase, in total, gives information about the shape of the wave [Maccarone, 2013].

As Herbers et al. [1995] and Ruessink [1998] proposed the the fraction of bound energy in the entire infragravity- frequency range is given by Eq 3.16.

$$E_{bnd}/E_{IG} = |b_{ii}|^2 \tag{3.16}$$

where $B(f_1, f_2)$ is the double integrated (between the IG and the short wave frequency bands) bicoherence estimation and $E(f)$ the energy density.

Eldeberky [1996] investigated extensively the non-linear wave interactions in shallow waters by using bispectral analysis. The cross-shore integrated bicoherence is shown in Figure 3.2. Bicoherence increases constantly over the shoaling area until the breaking point. Inside the surfzone, the bicoherence drops significantly, dictating the release of IG waves. On the other, hand biphase (Figure 3.3) remain steady as the wave shoals, due to the phase locked bound IG wave. Approaching the breaking zone, the biphase drops slightly due to the seaward free reflected IG waves [Sheremet et al., 2002]. Additionally in the surfzone, biphase decreases significantly, because of the IG release. At very shallow water (swash zone), the bicoherence starts to grow again when the biphase continues to drop [Michallet et al., 2014].
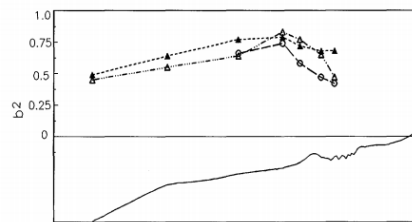
FIGURE 3.2: The spatial variation of the bicoherence over a beach for three wave conditions [Eldeberky, 1996].
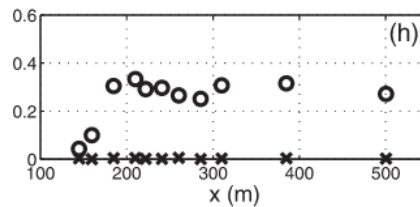
FIGURE 3.3: The biphases for the incoming (o) and outgoing (x) waves. Biphase is expressed in rads [Sheremet et al., 2002]

3.3 Evaluation of SWASH

The numerical model SWASH is presented extensively in the previous chapters, describing its fundamental equations. Scope of this section is to determine the limitations of SWASH in IG wave simulation.

SWASH solves directly the continuity and momentum equations (Eqs. 3.1, 3.2 and 3.3) in order to describe the free surface. That characteristic make SWASH able to simulate accurately phenomena like diffraction and refraction[Alabart et al., 2014]. Furthermore, due to the same characteristic, SWASH can deal with dyke geometry and porosity. So, SWASH can introduce partially reflective obstacles (or boundaries) to the domain, such as breakwaters [Zijlema et al., 2011].

An even more important feature of SWASH is that it can be run in multi-layered mode. This feature allows the model to simulate the computational grid divided into a number of terrain-following vertical layers. As a result, instead of increasing the frequency dispersion by increasing the order of the derivatives of the dependent variables (Boussinesq models), SWASH is able to account for that by increasing the number of the layers. Additionally, multi-layered SWASH is capable to simulate wave propagation even in deep areas, in contrast with the other depth averaged NSWE numerical tools. Table 3.1 shows that by increasing the number of the layers, K, the error of the calculations remain unchanged (even for large range of dimensionless depths).

TABLE 3.1: Range of dimensionless depth as function of number of layers K in SWASH

K	Range	Error
1	$kd < 0.54$	1%
1	$kd < 2.9$	3%
2	$kd < 7.7$	1%
3	$kd < 16.4$	1%

In addition, the current version of SWASH (2.00) accounts for wind effects on wave transformation in contrast with previous versions of the model and the air pressure at sea surface is optionally included. As a result, the simulation of storm surges based on space varying wind and atmospheric pressure can be carried out by SWASH.

According to literature there are researches [Buckley et al., 2014] which evaluate the performance of SWASH, related with IG waves. Buckley et al. [2014] determined that in a typical steep beach environment the model performs efficiently (slightly underestimates IG wave height), especially when the breaking parameters are tuned (Figure 3.4).

However, SWASH still has some lacks and limitations. Firstly, there is no option for (spatial) varied boundary conditions along the boundary layer. This means that (in
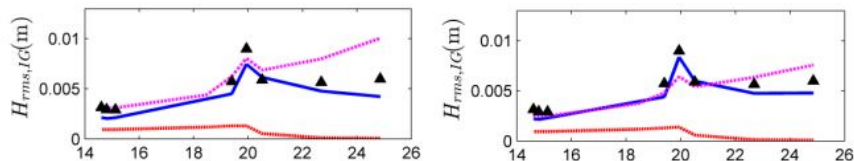
FIGURE 3.4: Measured (black triangles), and simulated $H_{rms,IG}$ and across fringing reef profile . Model results for untuned (left column) and tuned (right column) breaking parameters are shown for SWASH (solid blue curve), SWAN (dotted red curve), and XBeach (dashed magenta curve) [Buckley et al., 2014] .
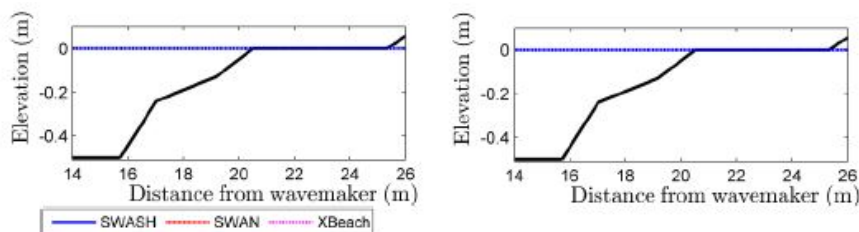
FIGURE 3.5: The reef elevation profile is shown in the bottom row for reference [Buckley et al., 2014] .

the boundary) although the water depth is different, the input wave conditions have to be stable (same characteristics) along to the boundary. This limitation can produce inaccuracies when the waves are not perpendicular to the boundary and the slope of the bottom is steep.

An additional drawback of SWASH is the way it models breakwaters. SWASH accounts for the characteristics of the breakwater, like the porosity, as the same for each vertical layer in the same spot of the domain. This assumption of SWASH leads to errors, especially when mound breakwaters are implemented. In addition the Forchheimer dissipative terms [Verruijt et al., 1970] are not included in the vertical momentum equations, as Mellink [2012] suggested.

Inaccuracies close to the shore could be caused by the high sensitivity of SWASH to the bottom friction variations, for the cases of mildly reflective IG wave conditions [Rijnsdorp et al., 2014]. This sensitivity could lead to the underestimation of the outgoing IG wave height. In such cases, roughness coefficient cannot be calculated a priori but there is a need of calibration in order to achieve higher accuracy of IG wave simulation.

Finally, at low vertical resolution, wave breaking is delayed [Smit et al., 2013] and high vertical resolutions are not feasible for large horizontal domains. So, the location of incipient short wave breaking (related with the breaking threshold) has consequences to the IG wave predictions (mostly overestimate the outgoing IG wave).

After an extensive investigation of SWASH limitations in the IG wave simulation, it is concluded that SWASH is a valuable tool, for scientific and engineering purposes, to

study the propagation of IG waves close to the shore. Advantages and drawbacks are summed up at Table 3.2.

TABLE 3.2: Advantages and drawbacks of SWASH

Advantage	Drawback
Simulate diffraction	Inaccuracies offshore boundary, no spatial variation
Partial reflection	Calibration of bottom roughness coefficient
Computational time reasonable	Inaccuracies in wave breaking
Includes wind effect	Same porosity of different vertical layers
Vertical layers	No Forchheimer dissipative terms

3.4 Conclusion

Advantages and drawbacks of SWASH are presented (Table 3.2). At this point, it is important to mention again that the objective of this thesis is to investigate the propagation of IG waves in a two dimensional case. Phenomena like diffraction and refraction are more dominant than breaking and the reflection from walls and breakwaters considered as partial. So, SWASH is the most valuable numerical model, in order to investigate IG wave propagation. SWASH is a valuable tool to simulate IG wave propagation in harbour domains and especially in the case of Barbers Point harbour. The reason is that it is capable of simulating all the phenomena that occur in shallow waters with environments where the properties vary rapidly.

Chapter 4

The two-dimensional case: Barbers Point Harbour

Barbers Point Harbor was constructed as a joint Federal and State project between 1982 and 1985. It is located close to Makaliko city on the island of Oahu, Hawaii, USA (Figure 4.1).

FIGURE 4.1: The location of Barbers Point harbour.

Barbers Point Harbour consists of by an entrance channel, a basin and a marina. The entrance channel is $140m$ wide, $1000m$ long and approximately $13m$ deep. The depth of the basin varies from $13.5 - 11.5m$ deep and it is $670m$ wide and $610m$ long, covering an area of $0.4km^2$. The private marina is $67m$ by $400m$ and the mean depth is $7m$. Rubble-mound wave absorbers line 1400 linear meters of the inner shoreline of the harbour basin.

Figure 4.2 shows a plan view of the near-shore profile at the Barbers Point Harbour area (including the basin and the private marina). The bathymetry is obtained by Zeki Demirbilek during a survey conducted at 1995. The bathymetry characterized as

uniform alongshore with steep slope in the offshore region (1:35) and mild slope in the near-shore area (1:200).
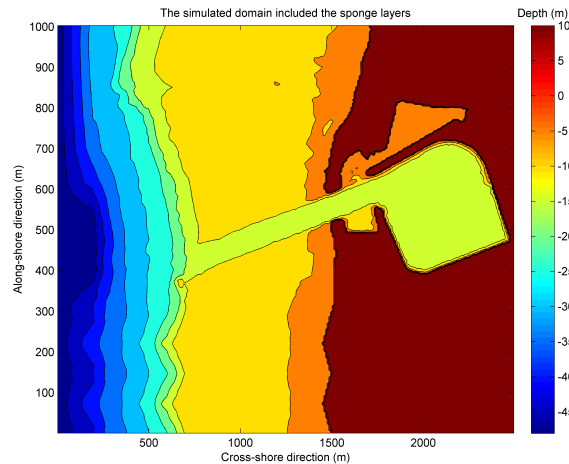
FIGURE 4.2: A plan view and the bathymetry of Barbers Point harbour.

4.1 Instrumentation

In the basin and in the entrance channel, there are several measuring devices, installed by CDIP, capable to measure the wave conditions (Figure 4.3). Most of them (especially inside the basin) are pressure sensors which are mounted at a fixed position underwater. These instruments measure pressure fluctuations - the changing height of the water column above the sensor - associated with passing waves. These pressure time series can be converted to sea surface elevations and wave frequency spectra. Although single-point gauges can effectively measure wave height and period, they cannot be used to determine the direction waves are traveling. Minority of the devices are directional buoys (e.g. 059-P1 and P6) which are capable to measure wave direction as well as wave energy.

The measuring devices, inside the basin of Barbers Point Harbour (066-P1, 066-P2 and 060-P3) were functional between $01 - 01 - 1987$ and $31 - 12 - 1989$. Simultaneously, buoys at the entrance of the channel (059-P1) and at the basin inlet (060-P2) were capable to take measurements for the wave conditions. Measurements from these five devices will be used in order to validate the model.
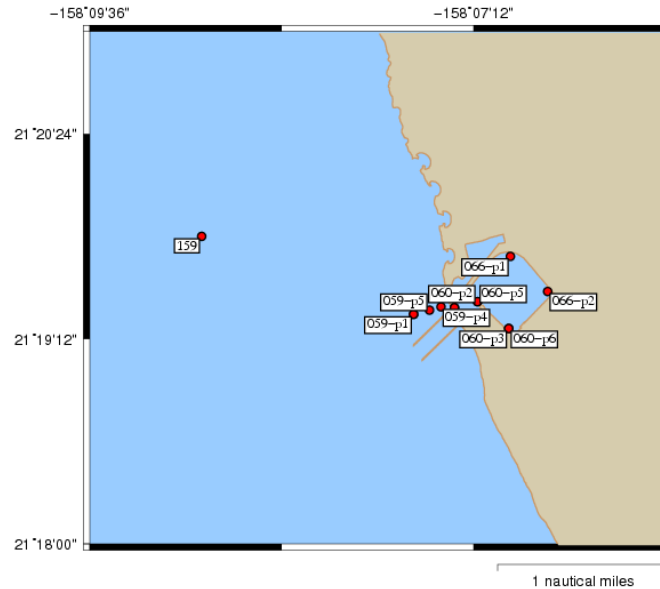
FIGURE 4.3: Location of different type of buoys, installed by CDIP around the Barbers Point harbour.

4.2 Wave measurements

As mentioned in Chapter 4.1, there is a restriction on the data. Devices are fully functional between $01 - 01 - 1987$ and $31 - 12 - 1989$. In this thesis, two data sets are considered (Figure 4.4 and Figure 4.5) . Each of the sets contains $7000sec$ of wave measurements, whereby the measurements started and finished at the time that Table 4.1 presents. Energy spectrums of the offshore boundary conditions and directional energy distributions are obtained by the master thesis of I.K. van Giffen [Van Giffen, 2003]. Each data set is considered as a separate case and the cases are identified by S16 and S17 (as the day of the incident).

TABLE 4.1: The duration and the date of the storm incidens

	Incident	Date	Time
incidents	S16	16/11/1989	19:26-20:46
	S17	17/11/1989	1:50-3:10

The considered offshore boundary conditions are derived from the measured wave conditions from the non-directional device buoy 159 (Figure 4.3), $3700m$ offshore to the entrance of Barbers Point Harbour.The device is located in a water depth of 80 m, providing data with sample rate $1Hz$.

The length of the given wave conditions (sample length) is considered acceptable and will lead to statistically accurate simulation of the IG waves. By using SWASH, some sort of equilibrium situation arises (under bi-chromatic waves) after 10 minutes of simulation. During these 10 minutes, the bound long wave has propagated from the offshore
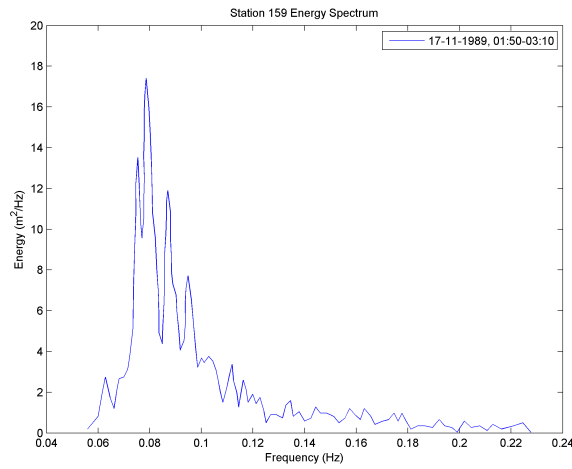
FIGURE 4.4: Offshore boundary energy condition (buoy 159) during the storm of 16-11-1989, 19:30-20:45. Sample length is 3900 seconds, sample rate 1 Hz and the mean direction is 260 degrees.
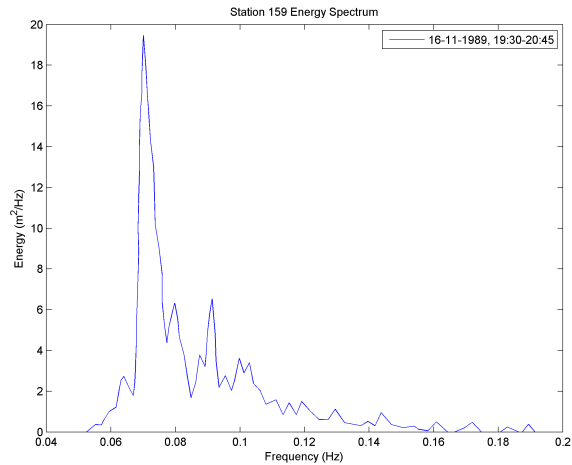
FIGURE 4.5: Offshore boundary energy condition (buoy 159) during the storm of 16-11-1989, 19:30-20:45. Sample length is 4800 seconds, sample rate 1 Hz and the mean direction is 275 degrees.

boundary to the harbour, has traveled across the basin, has been released as free infragravity wave and the equilibrium is arisen, as mentioned before. The length of the measured data has to be 80 minutes (10 until the equilibrium and 70 for the IG simulation) in order to achieve sufficient accuracy to enable high quality validation (simulate more than 100 infragravity waves) of the model.

4.3 Other characteristics of the harbour

The reflection of the infragravity waves on the structures is important for the overall wave pattern in the basin. In general, the reflected IG wave is considered much longer

than the obstacle (which causes the reflection) so the reflection is assumed as full. It is worth mentioning that this assumption will lead to overestimation for higher frequency waves.

Not much is known about the bed material for Barbers Point Harbour. The type of bottom material offshore is some sort of coral reef. For the case of Barbers Point harbour, mild reflection is expected due to the mild slope of the adjacent shore and bottom friction is not considered as a dominant dissipation mechanism for the incoming IG waves. However, inaccuracies are expected on the calculations of the outgoing IG waves as Rijnsdorp et al. [2014] identified.

Wave data was detrended over $1000sec$ intervals to remove tidal components. During the first part of the storm the tide was subsiding. During the second part the tide was at its lowest point. Tidal amplitude at the moment was around 0.35 cm. Because of this low tidal amplitude the influence of the tide on the outcome of the model is not taken into count. Slight errors in determined response frequencies could be the result of this assumption.

Finally, the meteorological data for the two different incident storms, S16 and S17, are given by the National Data Buoy Center. The wind regime is measured $70km$ away from the Barbers point Harbour and it is shown in Table 4.2. The wind speeds, for both of the cases, were remaining steady during the storm, according to the data provider.

TABLE 4.2: Wind speed during the investigated storms

Incident	Date	Wave speed (m/s)
S16	16/11/1989	11
S17	17/11/1989	12

4.4 Infragravity wave regime

At the measuring location 059-P1, the given surface elevation is decomposed to the IG wave and short wave component by using the FFT method. Aim is to present the infragravity regime outside the basin and identify the origin of the IG waves. Insight to the generation and propagation of the IG waves is given by using the cross-correlation function and determine the ratio of the bound and free IG waves at the specific location (059-P1).

As mentioned, surface elevation ζ is given at the buoy 059-P1. By using the frequency band $(0.005Hz < f < 0.05Hz)$ for the IG waves, ζ_{IG} and ζ_{hf}, for the IG waves and the short waves respectively, are extracted. The forcing of the IG-waves are related with the

variation of the wave amplitude and the wave envelope gives a measure of this amplitude variation. Hilbert transformation (Appendix A.1) is applied in order to calculate the wave envelope of ζ_{hf}. Finally, the cross-correlation (Appendix A.2) between the envelope and the IG surface elevation is calculated (Figure 4.6) in order to determine qualitatively the relation between the long and the short wave component. Aim is to provide a first view of the IG wave regime close to the harbour of Barbers Point.
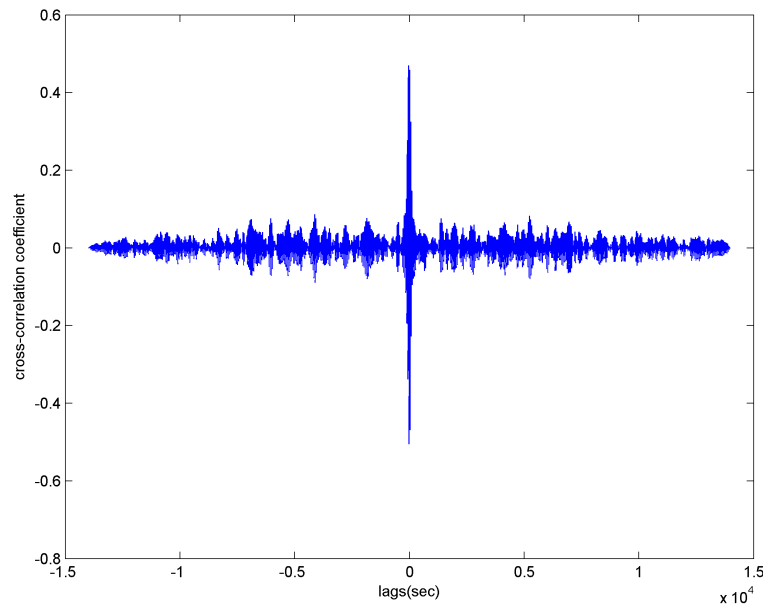
FIGURE 4.6: Cross-correlation coefficient between short wave envelope and IG wave surface elevation ζ_{IG} for the storm incident S16.

Cross-correlation with the Hilbert envelope dictates that (almost) the 60% of the IG waves (cross-correlation coefficient close to 0 lag) is related the short wave motion at the location 059-P1. As a result, the major part of the IG waves is generated by short wave interactions (at this point). However, the 40% of the IG waves seems to behave as free IG waves. It is assumed that the largest part of the free IG waves is caused due to the strong reflections on the vertical structures of the Barbers Point harbour. Finally, a minor part of this free IG wave is originated from the adjustment shore and propagates as an edge wave (Chapter 2.3). Cross-correlation provides a qualitatively and not quantitatively presentation of the IG wave regime at the offshore location.

4.5 Model setup

As it is mentioned in Chapter 3.4, SWASH [Zijlema et al., 2011] is used in order to simulate the IG wave propagation in the area of Barbers Point Harbour. In this section, the setup (for the specific case) of the model is presented.

4.5.1 Offshore wave conditions

The offshore boundary conditions, for the two incident storms, are well defined as non-directional wave energy spectrums by CDIP (Figure 4.4 and Figure 4.5). The directional spreading of the spectrum is is given in terms of the power m, where the $cos(\theta)^m$ distribution is assumed. The directional spreading is $m_s = 25$ and it is provided by [Van Giffen, 2003]. To conclude, the directional spectrums, for each storm incident, are presented in Figure 4.7 and in Figure 4.8.
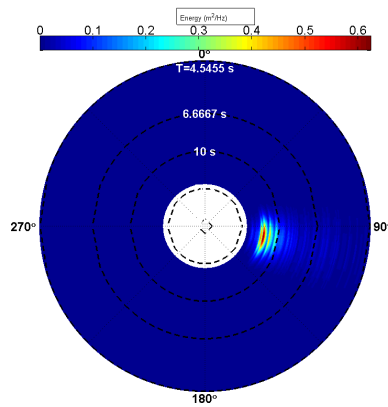
FIGURE 4.7: The directional spectrum at the offshore boundary which implemented in SWASH in order to simulate the storm incident S16.
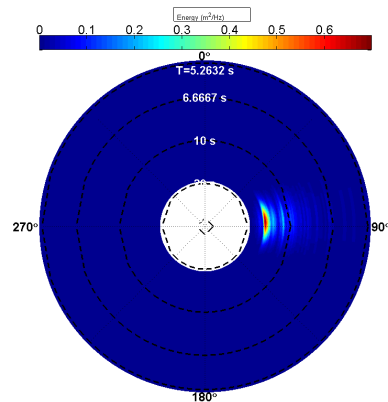
FIGURE 4.8: The directional spectrum at the offshore boundary which implemented in SWASH in order to simulate the storm incident S17.

4.5.2 Lateral boundaries

In SWASH, lateral boundaries are assumed as fully reflective and sponge layers have to be used (Chapter 3.1.2.3) to achieve weakly reflective lateral boundaries. The width

of the sponge layer has to be (at least) 3 times the typical wave length. For the case of Barbers Point harbour (for both the incident storms, S16 and S17) a typical wavelength of $70m$ and as a result, the sponge width of $200m$ is required. The area which is covered by sponge layers is presented in Figure 4.9. It has to be noted that the points of interest (measuring points) has to be outside of these sponge areas in order to prevent underestimations of IG wave characteristics.
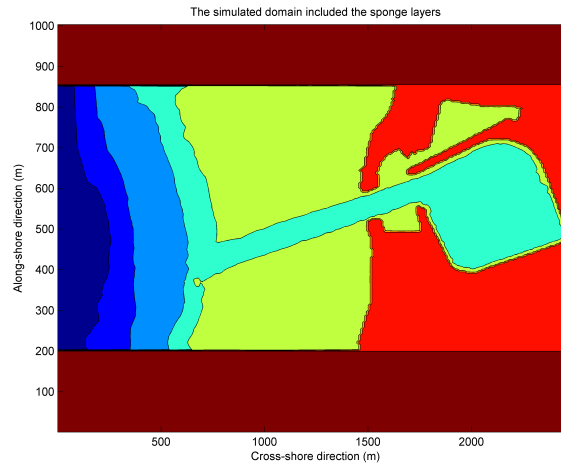
FIGURE 4.9: The sponge layers (areas covered by brown color) implemented in the simulated domain.

4.5.3 Other input parameters

The grid spacing is 3 x 7 m, in order to represent efficiently the propagation of IG waves and achieve reasonable computational time (roughly 1 day). The grid size should not become too high as short waves may disappear due to numerical effects (20 grid cells per wave length [Swa]). Additionally, grid is simulated as rectangular and constant through the domain. Furthermore, in order to obtain stable simulations the time step is set at 0.02 s and the maximum Courant number at 0.8.

With regard to the vertical layers, SWASH developers define that the number of the vertical layers depends on the wave number, k (so the wavelength, L, as well) and the water depth. The relationship between these parameters is shown on the Table 3.1. In this study dimensionless depth is determined as kd $\approx$ 6 and the usage of two vertical layers is needed in order to avoid inaccuracies of the shorter wavea (which generate the IG waves).

Finally, some other modeling assumptions are presented. As it is mentioned, the influence of the tide is neglected which leads to slight errors. Furthermore, vertical structures and the adjacent shore is considered as fully reflective for the large wave-lengths of IG

waves. Additionally, the minimum simulated depth is considered as 0.3 m in order to prevent instabilities. This characteristic has no effect inside the basin (or outside) but it will lead to inaccuracies close to the shore-line.

Chapter 5

Sensitivity analysis and model validation

As it is mentioned, the input data (offshore wave conditions) for modeling are provided, partially from the CDIP and by [Van Giffen, 2003]. In order to proceed, the rest of the input data (offshore directional spreading and model setup parameters) are calculated and their sensitivity on the calculations are determined in Chapter 5. The effect of the parameters in Table 5.1 tuning is tested in SWASH. The tuned characteristics of the IG waves (in terms of wave energy spectrum and significant wave height, $H_{IG,sig}$) are compared with the observed IG wave measurements at the location 059-P1, outside of the basin (Figure 4.3). The comparison is carried out for the frequency band of the IG long waves (0.005 Hz- 0.05 Hz). After the determination of the Table 5.1 parameters, the IG wave behavior is presented and compared with the measured one inside the basin. Finally, the predictive skill of SWASH is calculated. In Chapter 5, the sensitivity analysis and validation is carried out only for the wave condition S16, whereas results for the wave condition S17 are presented in Appendix B.

5.1 Sensitivity Analysis

Despite the amount of data which are provided by CDIP and [Van Giffen, 2003], there are some input modeling parameters which are unknown a priori. These parameters are presented in Table 5.1 and they lead to simulation uncertainties. The sensitivity of SWASH will be investigated only for the parameters/ characteristics:

1. Directional Spreading, m_s

2. Width of sponge layers

3. Computational resolution (grid size)

4. Dissipation coefficient, β

5. Number of vertical layers

These specific parameters were chosen over other parameters because the lateral are assumed to have minor effect on the IG wave behavior inside the basin of Barbers Point harbour. As noted, tide effect is neglected and the structures are acting as fully reflective for the IG waves. Furthermore, the bathymetry around the Barbers Point harbour is characterized by mild slopes (close to the shore), leading to low shore reflections. As Rijnsdorp et al. [2014] determined, the bottom friction influences only the outgoing IG waves and for this case the investigation of the model sensitivity due to the friction coefficient can be neglected.

TABLE 5.1: Non-given parameters. With **V** are marked the parameters which are included to the sensitivity analysis an with **X** the parameters which are neglected

Parameters	Description	Sensitivity an.
Directional spreading	The directional distribution of the energy	**V**
Sponge layers	The width of the absorbers at the lateral boundaries	**V**
Grid size	The size of the rectangular computational grid in alongshore and cross-shore directions	**V**
Vertical layers	Number of computational vertical layers. Each layer covers a covers a constant percentage of the depth at a specific location	**V**
Water level	The initial surface level affected by tide	**X**
Dissipation coefficient	The breaking parameter β	**V**
Porosity size	The value of the porosity size related with the vertical structures	**X**
Friction coefficient	The bottom friction coefficient which is related with the dissipation of the waves	**X**

5.1.1 Directional spreading

The offshore boundary directional distribution of the energy is not measured by CDIP due to the absence of a directional buoy at the specific location (159 buoy). As mentioned (Chapter 4.5.1), the directional spreading is provided by [Van Giffen, 2003] in terms of power m_s. However, the directional spreading is further investigated in order to determine the validity of the provided distribution.

As Bowers [1992] determined, there is a strong correlation between the amplification of the bound IG waves (in terms of significant wave height, H_{sig}) and the directional

spreading. Bowers [1992] proved that the spreading is disproportional with the height and the length of the bound IG waves.

FIGURE 5.1: The IG wave energy spectrum for different values of directional spreading at the location 059-P1. Blue is the measured form CDIP, green for m_s=10, red for m_s=15, cyan for m_s=20, magenta for m_s=25 and yellow for m_s=40.

TABLE 5.2: The IG wave significant height for different directional spreading values compared to the observed one.

Directional spreading, m_s	Significant IG wave height, $H_{IG,sig}$ (m)
Observed	0.23
10	0.20
15	0.21
20	0.21
25	0.22
40	0.26

As it was expected, the IG wave significant height, $H_{IG,sig}$, decreases as the spreading increases (m_s decreases). Figure 5.1 shows that directional spreading has a strong effect to the increase of the IG wave energy at the location 059-P1. The observed IG wave significant height,$H_{IG,sig}$, is 0.23m. So, this research agrees with [Van Giffen, 2003] that a reasonable value for the directional spreading is $m_s = 25$. Slight mismatching, between the observed spectrum and the calculated for the $m_s = 25$, is caused because of these following reasons:

1. The IG wave frequencies lie below the conventional range of commonly deployed wave measurement devices

2. The location of the buoy 059-P1 is not provided but it is approximated from Figure 4.3

5.1.2   Sponge layers

As described in Chapter 3.1.2.3, lateral boundaries have to act as an open free bound-
aries. In SWASH model they can be implemented as fully reflective and their location
has to be determined in order to reduce their effect in the area of interest (in this project
inside and close to the basin of Barbers point harbour). Additionally, the schematization
of sponge layers at the lateral boundaries is suggested (by the developers of SWASH)
in order to describe more accurately the proper behavior of the lateral boundaries. The
sponge layer's length has to be 3 times the average wave length, in order to absorb the
energy of the waves.

In this case, the typical wave-length is calculated as $70m$ and the width of sponge layers
of $200m$ is used (Figure 4.9). However, the length of the IG waves are longer than the
$70m$. Different widths (Table 5.3) of sponge layers are used and the simulated (for each
width) IG wave significant height, H_{sig}, at the location 059-P1 is compared with the
observed one. Defining the proper width of sponge layers is crucial for this case because
the width is related with the computational time. As the width increases, the domain
has to be expanded and the simulation time raises. On the other hand, as the width
decreases, the reflectivity of lateral boundaries grows, as well.

FIGURE 5.2: The IG wave energy spectrum for different values of sponge layer width,
at the location 059-P1. Blue is the measured form CDIP, green for *spon*=0 m, red for
spon=100 m, cyan for *spon*= 200 m and magenta for *spon*= 400 m .

The energy spectrum (Figure 5.2) and the IG significant height (Table 5.3) are calculated
for different directional spreading values at the location 059-P1. Table 5.3 dictates, the
optimum value of the sponge layer width is $200m$. For lower values, the area is affected
by the reflected waves from the lateral boundaries. In contrast, for larger sponge widths
there is no effect at the location 059-P1. The lateral boundaries, covered by a sponge

TABLE 5.3: The IG wave significant height for different sponge layer widths compared to the observed one.

Sponge layer width (m)	Significant IG wave height, $H_{IG,sig}$ (m)
Observed	0.23
0	0.55
100	0.31
200	0.22
400	0.22

layer of 200 m (3 times the typical wave length) act like absorbers or weak reflective boundaries.

5.1.3 Grid size

As mentioned in Chapter 4.5.3, the typical wave-length has to be 20 times larger than the grid size according to the manual of SWASH. So, the computational grid has to be at least 3.5 m x 3.5 m (the average wave length is $70m$). However, this research is focused in IG waves with larger wave lengths. The variations to the computations due to the used grid size are investigated. It is expected that higher resolutions will lead to over-estimations and a sensitivity analysis is required in order to determine the optimum grid size.
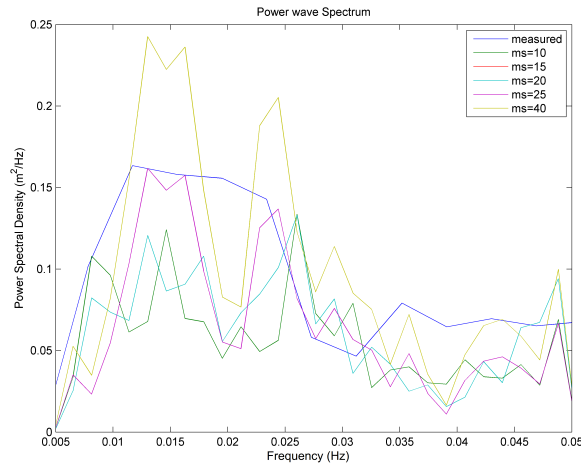

FIGURE 5.3: The IG wave energy spectrum for different values of grid size resolution, at the location 059-P1. Blue is the measured from CDIP, green for 1 vertical layer and red for 2 vertical layers.

The optimum grid size considered the 3 m x 7 m (Figure 5.3). Lower computational resolution leads to overestimations and the higher to high computational time with a significant change to the IG wave regime (Table 5.4).

TABLE 5.4: The IG wave significant height for different grid sizes compared to the observed one.

Grid size (Alongshore direction x Cross-shore direction)	Significant IG wave height, $H_{IG,sig}$ (m)
Observed	0.23
6 m x 14 m	0.55
3 m x 7 m	0.31
1.5 m x 3.5 m	0.22

5.1.4 Vertical layers

The vertical separation of the domain in layers is the innovative feature of SWASH compared to the other wave numerical tools. As defined in Chapter 4.5.3, the vertical layers has to be 2 in in order to prevent inaccuracies in depths larger than $30m$. At this high-depth locations the waves interacting between its other but the "strength" of these interactions are low. The amplification of bound IG waves becomes significant when the wave group propagates through depths lower than 15 m, where the use of one vertical layer is considered reasonable. Fluctuations of the IG wave calculations (at the measured locations) due to the number of vertical layers are determined for the case of Barbers Point harbour. Unfortunately, SWASH becomes unstable when the vertical domain is separated in 3 layers, especially close to the structures.
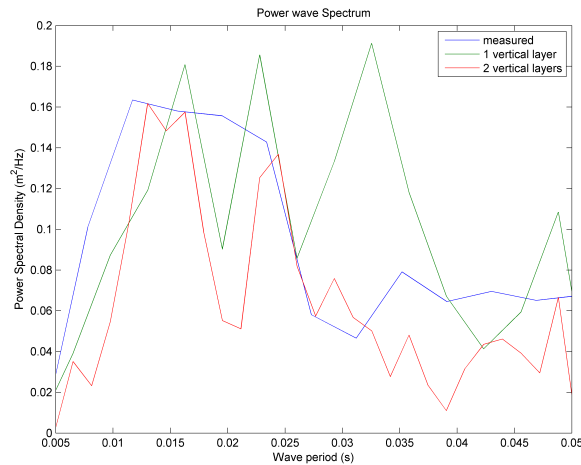
FIGURE 5.4: The IG wave energy spectrum for different number of vertical layers, at the location 059-P1. Blue is the measured form CDIP, green for 1 vertical layer and red for 2 vertical layers.

TABLE 5.5: The IG wave significant height for different grid sizes compared to the observed one.

Number of vertical layers	Significant IG wave height, $H_{IG,sig}$ (m)
Observed	0.23
1 vertical layer	0.28
2 vertical layers	0.22

At this point, it has to be mentioned that the number of vertical layers is related with the computational resolution, similar to the the grid size. As explained in the previous Chapter 5.1.3, when the resolution becomes coarser, SWASH tends to overestimate the characteristics of the IG wave (Figure 5.4 and Table 5.5).

5.1.5   Breaking parameter

The default value dissipation coefficient, α, which controls the wave breaking is 0.6 and it is considered reasonable both for irregular and regular waves over mild bathymetries. However, for steep bathymetries the value of β has to be reduced. In the case of a harbour, breaking phenomenon is not significant. However, there is a possibility to have significant contribution to the IG wave energy by edge waves (Chapter 2.3) which are related to the breaking phenomenon and generated at the adjacent beach.
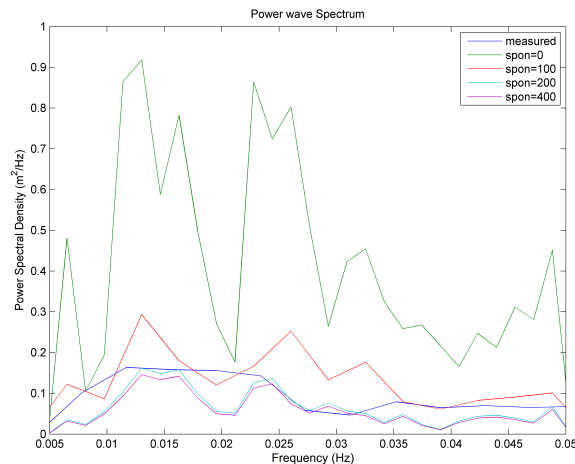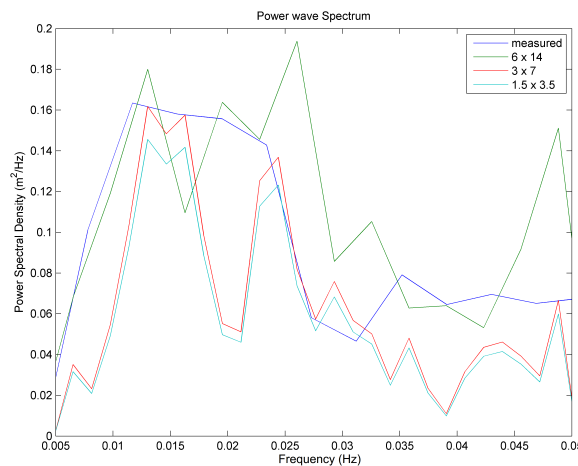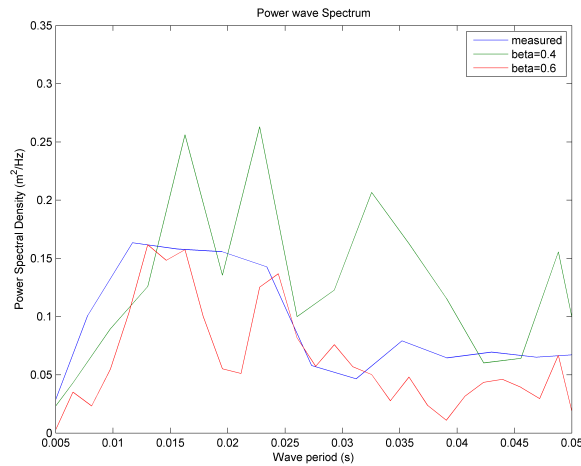

FIGURE 5.5: The IG wave energy spectrum for different dissipation coefficient, at the location 059-P1. Blue is the measured form CDIP, green for $\alpha = 0.4$ and red for $\alpha = 0.6$

TABLE 5.6: The IG wave significant height for different grid sizes compared to the observed one.

Dissipation coefficient, α	Significant IG wave height, $H_{IG,sig}$ (m)
Observed	0.23
0.4	0.31
0.6	0.22

Reduction of the breaking parameter β leads to overestimation of the IG wave energy density (spectrum) (Figure 5.5) and the IG significant height (Table 5.6). The short waves tend to break earlier, the surf zone expands and the edge waves are amplified. This phenomenon increases the IG wave height, $H_{IG,sig}$ at the location 059-P1.

5.2 IG wave inside the basin

The set-up of the numerical model, SWASH, is aimed to simulate accurately the behavior of IG waves inside and close to the basin of Barbers Point harbour. Partially, the model input parameters and characteristics are given from the CDIP and [Van Giffen, 2003]. Although, some of these parameters (Table 5.1) are not provided and has to be assumed and tested (by using the sensitivity analysis) in order to achieve accuracy. The tested, non-given, parameters are presented in Table 5.7 with their values as they determined by the sensitivity analysis. These values of the parameters (Table 5.7) are used in order to simulate the area inside the basin of Barbers Point harbour (for both of the wave conditions, S16 and S17).

TABLE 5.7: The input parameters as defined apriori and tested in the sensitivity analysis

Parameter	Value
Dissipation coefficient (β)	0.6
Directional distribution, m_s	25
Vertical layers	2
Grid size	3 m x 7 m
Sponge layer	200 m

In Figure 5.6 measured energy spectra are compared with the simulated by SWASH. The numerical model seems to perform accurately for the case of Barbers Point harbour. In general, SWASH tends to overestimate IG waves in the basin, slightly. However, the frequency components of the IG waves seems to be calculated accurately for the four measuring points inside the Barbers Point harbour.

Several spikes at the energy spectrum, mostly at multiples of 0.008 Hz, reveal that resonance is induced inside the basin due to the presence of IG waves (Appendix C). Figure 5.7 shows the IG significant wave height,$H_{IG,sig,calc}$ inside the basin calculated by SWASH. Circled points are the CDIP measuring devices (Figure 4.3) and inside the circle, the measured IG significant wave height, $H_{IG,sig,meas}$, is presented. It is observable that the assumed locations of the buoys inside the basin are considered accurate.

5.3 Predictive skill of SWASH

Reniers et al. [2002] defined the predictive skill with the following equation:

$$Skill = 1 - \sqrt{\frac{< (H_{IG,sig,meas} - H_{IG,sig,calc})^2 >}{< H_{IG,sig,meas}^2 >}} \qquad (5.1)$$
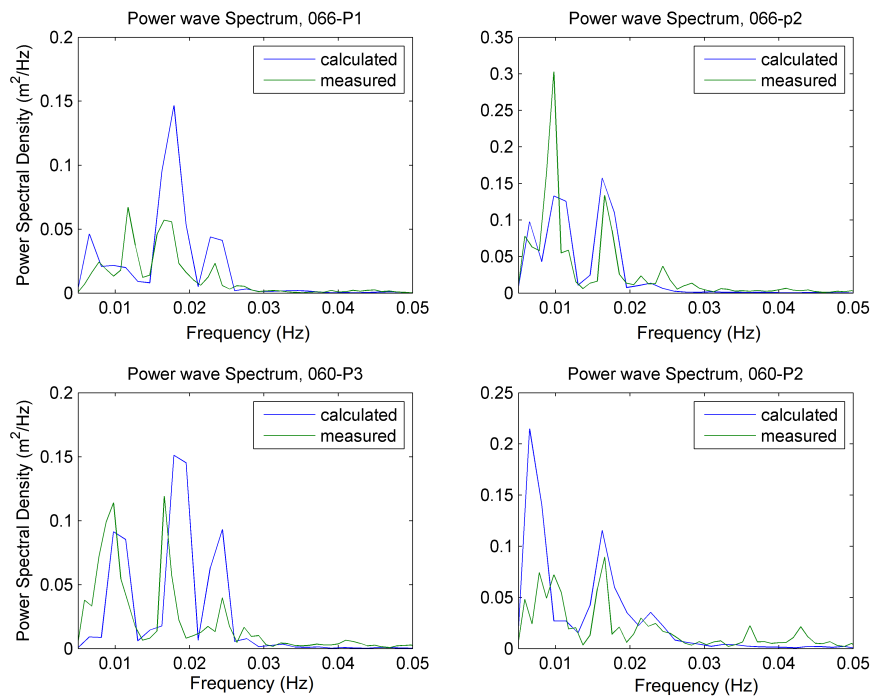
FIGURE 5.6: Energy spectrums calculated at different locations, 066-P1,066-P2,066-P3 and 060-P2 compared with the measured spectrums by CDIP.
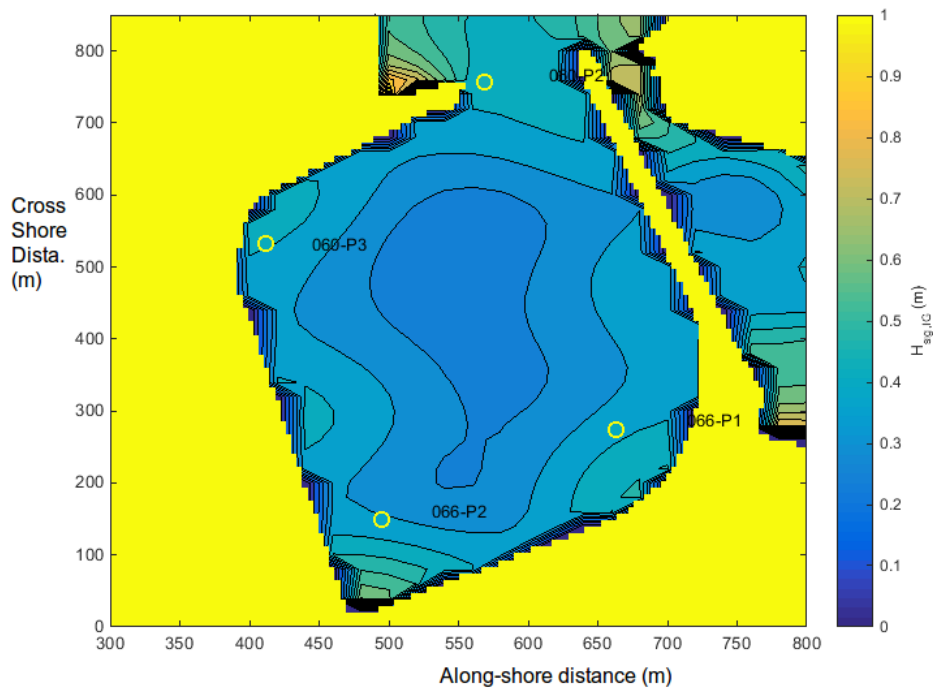
FIGURE 5.7: The significant IG wave height inside the basin as it is calculated by using SWASH. The circles represent the measured locations and inside the circles the value of the IG significant height is the measured one.

$H_{IG,sig,meas}$ is the measured significant height and $H_{IG,sig,calc}$ is the calculated significant IG wave height. The predictive skill gives an indication of the magnitude of the difference between the measurements and the predictions relative to the measured value. For a skill of 1 the difference is zero, while for a value of 0 the difference is equal to the measured value. The results show that SWASH is capable of predicting the IG-wave conditions at a specific site with an average skill of 0.84. The predictive skill is 5 % higher than Reniers et al. [2010] and Rijnsdorp [2011] calculated by using IDSB [Reniers et al., 2002] and SWASH respectively. It was expected a high predictive skill of the numerical model, due to the usage (for this project) of the newest (2.00) and more validated version of SWASH.

Chapter 6

Separation of the Infragravity waves

As mentioned in Chapter 1 and Chapter 2, IG waves are generated by non-linear interactions of short waves in the shoaling area (seawards of the breaking zone). Going deeper, to the field of IG wave origins, Longuet-Higgins and Stewart [1962] identified that a pair of short waves with relatively close frequencies, f_1 and f_2, tends to generate a bound and "out of phase" wave with frequency, $f_1 - f_2$, due to mass and momentum fluxes modulations with the short wave groups.

Bispectral analysis is a valuable tool in order to investigate the boundness between the short and the IG waves (Chapter 3.2). In this thesis, measurements of surface elevation (at several locations) are used to obtain the linear, the non-linear energy fluxes and the energy transfers between the short and IG waves based on the equations of Ruessink [1998](Chapter 3.2). Additionally, the IG wave signal is decomposed to the incoming and outgoing component by using the Sheremet et al. [2002] method (Chapter 2.3).

6.1 Methodology

6.1.1 Description of the domain and the wave conditions

The investigated domain is the Barbers Point Harbour (Figure 4.2). The offshore wave condition is the storm on 16 of November 1988, presented in Chapter 4.2. Focus is given on one offshore wave condition (S16) in order to understand and analyze in depth the IG wave complex behavior. Finally, the numerical model (SWASH) set-up remains the same as it was determined partially in Chapter 4 and, after an extensive sensitivity analysis, in Chapter 5.

The breaking zones are presented in Figure D.1 for the wave conditions S16. Breaking zones are calculated by using SWASH. The numerical model provide (as an output) a the spatial variation of a certain parameter in the of the simulated domain, masking the breaking points as 1 and non-breaking points as 0. According to the bore concept, wave breaking occurs outside of the basin, west and east to the harbour inlet. As mentioned in Chapter 4.2, related to the characteristics of the wave condition S16, the estimation of the breaker zones is coming from $65min$ wave simulation. The simulated breaking zones (Figure D.1) (by SWASH) are compared with the breaking zones (Figure D.2) (for the same wave conditions) calculated by the Weggel [1972] breaking criterion (Appendix A.3) in order to identify the validity of SWASH to simulate accurately the breaking phenomenon.

Finally, the analysis (Chapter 6.1.2) of the IG waves is taking place only outside of the Barber Point harbour. The decomposition of IG waves, by using bispectral analysis, leads to inaccuracies inside the harbour basin due to the basin's resonance. Standing waves (caused by resonance) will cause an increase of the bicoherence, unrelated to the IG wave behavior, as Dong et al. [2010] mentioned. Furthermore, the results of the analysis are presented for two 1D beach profiles (**PBr** and **PIn** profile in Figure 6.2), and their characteristics at Table 6.1), in order to simplify the interpretation. Both of them (the profiles) are arrays, following the (mean) wave crests and are shown in Figure 6.1. **PBr** profile is chosen because it includes phenomena like shoaling (over steep and mild slope bathymetry) and breaking phenomena, which have significant effect on the IG wave behavior (Chapter 2). **PIn** profile is more important from an engineering point of view, as it includes the inlet and the entrance channel. Aim is to determine the magnitude and the nature (free or bound IG waves) of the IG waves which are penetrating into the basin.
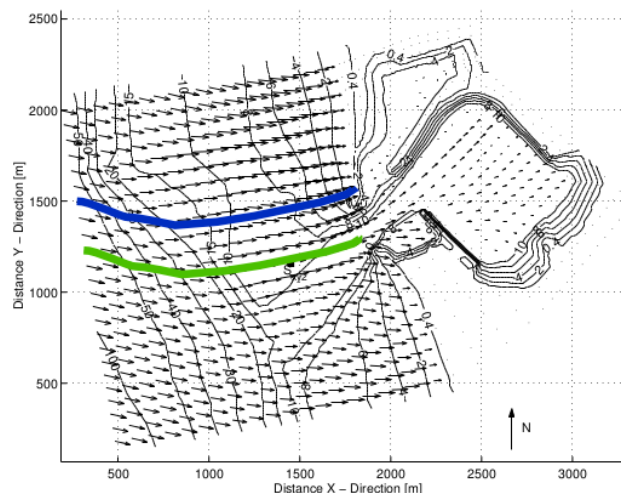
FIGURE 6.1: Location of the simulated transects, PBr (blue) and PIn (green). Arrows show the mean direction of the waves (total wave signal) for the S16 wave condition.
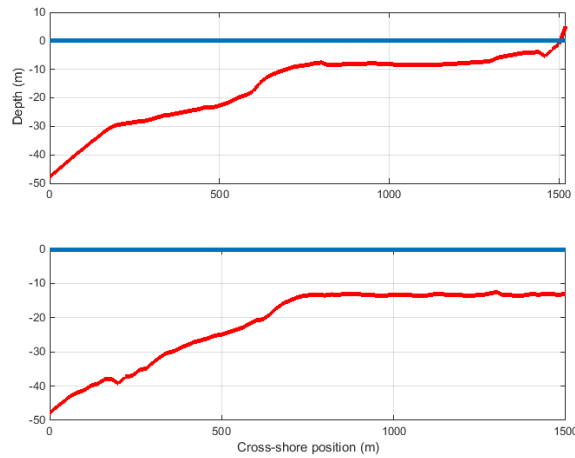
FIGURE 6.2: The bottom profiles, PBr (upper panel) and PIn (bottom panel). With red color is the bottom profile and with blue the mean water level.

Simulated Profile	Discrete Zones	Cross-shore Distance (m)	Simulated Profile	Discrete Zones	Cross-shore Distance (m)
PBr	Steep-slope	0 -600	**PIn**	Steep-slope	0 -600
	Mild-slope	600 -1200		Entrance Channel	600 -1400
	Offshore to the breaking point	1200 -1300		Close to the inlet	1400 -1500
	Breaking zone	1300 -1400			
	Surf Zone	1400 -1500			

TABLE 6.1: Separation of the profiles **PBr** and **PIn** to discrete zones

6.1.2 Analysis

The first objective of the IG wave analysis is to separate the low from the high frequency signal (Chapter 6.2.1). The FFT method (Chapter 3.2) is applied to the surface elevation signal (recording frequency, $f = 10Hz$) and frequency band filters are applied (IG waves frequency between 0.005-0.05 Hz and short wave frequency between 0.05-0.25 Hz). A separation of the high-low signal and calculation of their characteristics (i.e. H_{sig}, energy) shows the origin and the propagation of the IG waves.

One step forward to this analysis is the decomposition of the IG wave signal (Chapter 6.2.2). As mentioned in Chapter 1 and Chapter 2, IG waves are consisted by two components, the bounded and the released (free) and for their decomposition, the bispectral analysis is used. The frequency bispectral resolution is $0.0003Hz$ and the time series are segmented in $1000s$, 50% overlapping sections, that are detrended and tapered by using the Hanning window. Double integration (between the IG and the short wave frequency bands) of bicoherence determines the ratio of the bounded IG waves (Chapter 3.2).

Continuing to a further analysis, the IG wave signal is decomposed to the incoming and outgoing IG wave. The separation method of Sheremet et al. [2002] is applied (Chapter 2.3). For this particular method, the cross-spectrum of the velocity and surface elevation signal with recording frequency, $f = 10Hz$, is used.

6.2 Results

6.2.1 Separation of the total signal

In this chapter, the total signal is decomposed to the short waves and the IG waves. Figure 6.3 and Figure 6.4 present the spectral evolution for the **PBr** profile and the **PIn** profile, respectively. Starting with the **PBr** profile, the energy seems to be concentrated between the first order components (same components as the off-shore wave conditions, Figure 4.4) at *the steep-slope zone*. As the waves propagates through the *the mild-slope zone* the short waves tend to dissipate and transmit their energy to the second-order components, generating the IG waves (location $x = 700m$, Figure 6.3, upper panel). As the waves continue the shoaling, primar short wave frequency components, f_{p1} and f_{p2} (for the S16 wave condition $f_{p1} = 0.08Hz$ and $f_{p2} = 0.1Hz$, Figure 4.4) tend to interact and produce sub-harmonics ($f_{sub} = f_2 - f_1$). The interactions start with the primar component (Figure 6.3, sub-harmonic pops-up with $f_{sub} = f_{p2} - f_{p1} = 0.02Hz$) and continue with the rest short wave components. So, the distribution of the IG wave energy becomes broader as the wave propagates from the IG wave generation point (location $x = 700m$) to the shore. Furthermore, the energy (in average) of the IG wave increases constantly, as the waves come closer to the shore. The peak of the IG wave energy is located at the *surf zone*. The evolution of the IG wave significant height, $H_{sig,IG}$ (compared to the short wave significant height, $H_{sig,SW}$) is presented in Figure 6.5 in order to provide a better view of the IG and short wave (average) energy at any location. Finally, both Figure 6.3 and Figure 6.5 show that there is no IG wave breaking at the surf zone because of no IG energy dissipation in this area (*surf zone*).

Continuing to the energy evolution for the **PIn** case, Figure 6.4 shows similar trend to Figure 6.3, at *the steep-slope zone*. The presence of IG waves occurs in the *entrance channel zone* where the energy of the short waves is almost nullified. Obviously, in the **PIn** profile, IG waves are not generated by transmission from the first-order components to the second-order terms (IG waves). Short waves are reduced shore-wards of the location, $x = 900m$, and the IG waves are generated after the location, $x = 1100m$. Additionally, the IG waves are introduced in the domain covering a broad frequency band (broader than the **PIn** IG frequency band at the generation point) and this frequency

FIGURE 6.3: The spectral evolution, in terms of variance energy density (m^2/Hz). The upper panel dictates the energy distribution for the IG waves, ($0.005 - 0.05Hz$), and the bottom panel the energy distribution for the short waves,($0.05 - 0.25Hz$). Both of the panels are showing the energy evolution for the profile **PBr**

band remains, relatively, constant through the domain. So, there is no transmission to the sub-order harmonics similar to the **PBr** case. This dictates the generation and amplification of the IG waves in areas outside of the presented, **PIn**, domain (*the mild-slope zone* of the adjacent area). Finally, the sharp decrease in the short wave energy (Figure 6.5, bottom panel) at the area $x = 600 - 1000m$ is caused by refraction due to the entrance channel. Short wave tends to leak through the sides of the channel to the adjacent area, when the IG wave are strongly refracted into the channel.

Finally, the IG wave direction of propagation is compared to the direction of short waves and it is presented in Apppendix D. The directional spectrums are constructed for the low and the high frequency components, for different locations of both the profiles, **PBr** and **PIn**.

6.2.2 Decomposition of IG waves

Bispectral analysis showed non-linear transfers of energy for both, **PBr** and **PIn** profiles. These energy transmissions are amplified across the shoaling areas and reduced due to breaking phenomena. Figure 6.6 shows an example of the normalized bispectrum (bicoherence) at several locations. Normalized bispectrum examples are presented only
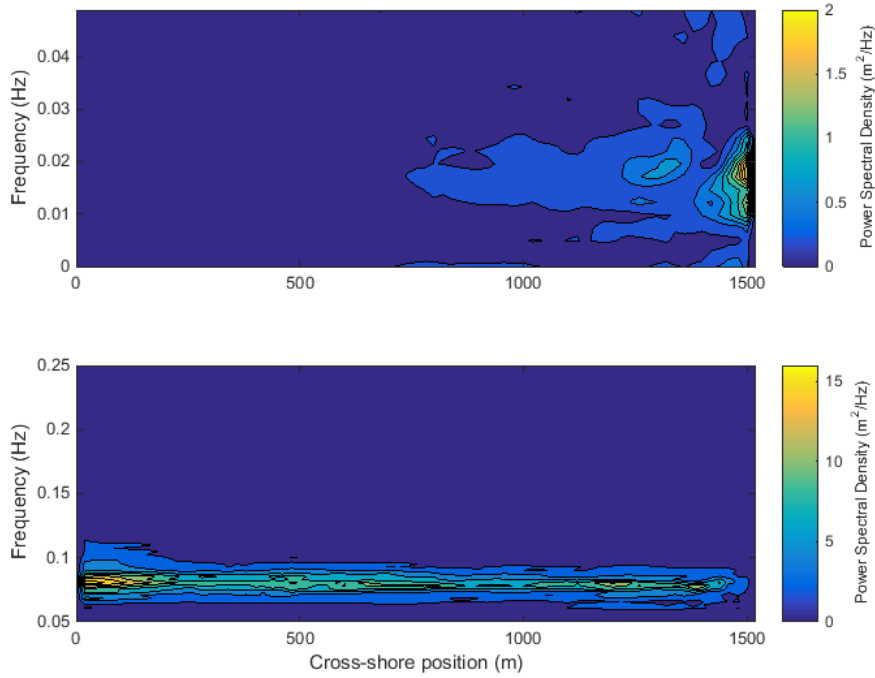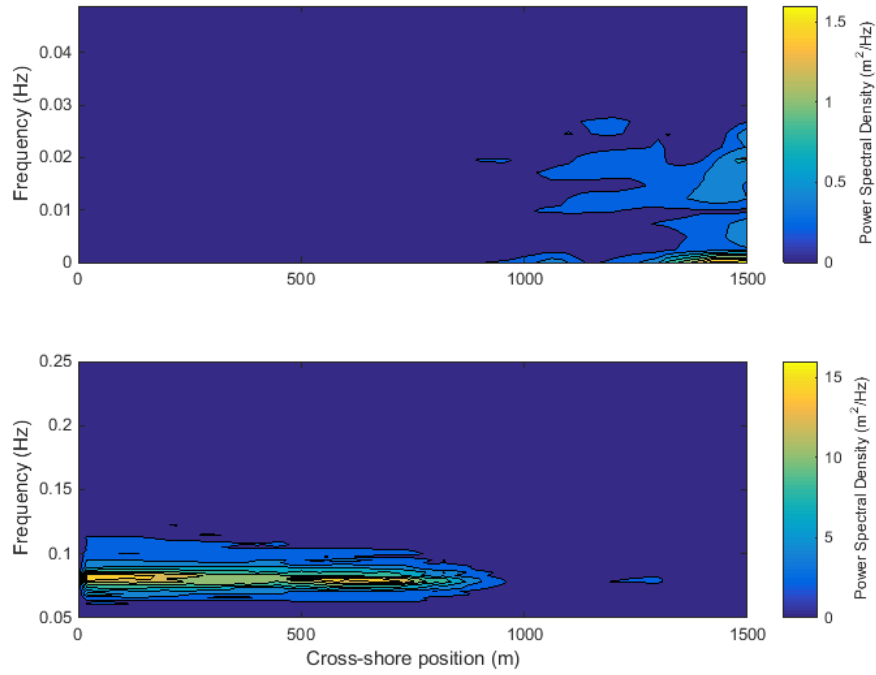
FIGURE 6.4: The spectral evolution, in terms of variance energy density (m^2/Hz). The upper panel dictates the energy distribution for the IG waves, ($0.005 - 0.05Hz$), and the bottom panel the energy distribution for the short waves,($0.05-0.25Hz$). Both of the panels are showing the energy evolution for the profile **PIn**

FIGURE 6.5: The significant height for the IG (red color) and short waves (blue color). Upper panel is the **PBr** profile and the bottom panel the **PIn** profile.

for the profile **PBr**, whereas examples for the **PIn** profile are included in the Appendix F. Starting with the upper-left panel in Figure 6.6, non-linear interactions are observed in the sea-swell and the IG band. These interactions are not taking place only between the wave peak period, $f_p(=0.09$ Hz) and the frequencies of IG waves, but also between the higher harmonics (nf_p, n is an integer) and the IG waves. As the wave propagates the energy transfers are increased, due to shoaling (upper-right panel in Figure 6.6).

At the *breaking zone*, ($x = 1200m$, bottom-left panel in Figure 6.6) the interactions between the short and the IG waves become scattered and their behavior is hard to interpret. At this location, high energetic short waves brake and lower energetic short waves continue to shoal. However, in the *surf-zone* ($x = 1480m$,bottom-right panel in Figure 6.6), the bicoherence reduces significantly, indicating that the IG wave component is no longer forced by the short waves.
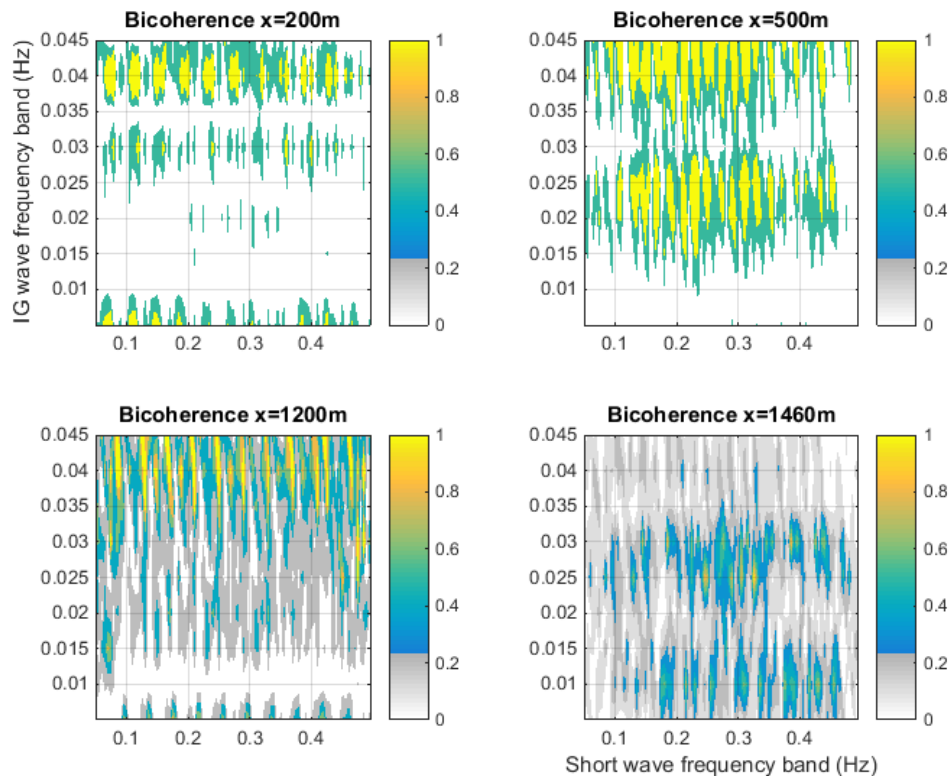
FIGURE 6.6: Examples of the normalized bispectrum for different locations, for the **PBr** profile.

The evolution and fluctuation of the integrated bicoherence (Figure 6.7) and the integrated biphase (Figure 6.8) across the profiles **PBr** and **PIn** can provide a better view of the IG wave behavior. Integrated bicoherence ($|b_{ii}|$) and biphase ($|\theta_{ii}|$) were calculated for each bispectrum, by averaging $b(f_1, f_2)$ and $\theta(f_1, f_2)$ over $[f_1, f_2]=[0.005-0.05,0.05-0.2]$.

For both the profiles (**PBr** and **PIn**) the IG regime is similar at the *steep-slope zone*. At the beginning, IG waves have low energy amplitude, due to the large depth, and are continuing to shallower waters, where the bound IG waves are amplified. When the wave is introduced to the *mild-slope zone* a decrease of the bicoherence occurs for both of the cases. This behavior dictates a slight release of the IG waves due to the slope change. The generation of free IG waves can be observed in Figure 6.7, as well ($x = 550m$).

For the **PBr** profile, the bicoherence remains steady as the toatal (IG and short) wave propagates to the *breaking zone*. Close to the breaking point, bound IG wave seems to be dominant ($|b_{ii}| > 0.7$). Moving further to the *surf-zone* the bicoherence drops sharply, the biphase decreases and the bound IG waves are released. The boundness of IG and short waves is slightly increased again in the shallower waters ($1450 - 1500m$) of the *surf-zone*. The biphase (Figure 6.8, upper panel) remains constant ($\theta = 177^o$) until the breaking point. Passing that point and reaching the breaking zone, the biphase drops from $\theta = 177^o$ to $\theta = 160^o$ (in the surf zone), dictating the release of IG waves due to breaking phenomena.

In contrast with **PBr**, **PIn** bicoherence does not show any severe fluctuations at the *entrance channel zone*. The reason for that steady ($b = 0.32 - 0.36$) behavior is the flat bathymetry. Only after $x = 900m$ bicoherence drops by 0.1 and reaches again the previous ($b = 0.32 - 0.36$) value after $x = 1400m$. This fluctuation is caused by the effect of refraction, due to the entrance channel. Long waves are strongly refracted inside the basin when the short waves propagate to the adjacent shore. This phenomenon cause the release of IG waves and the slight drop of the bicoherence.

Finally, the free and bounded IG wave components are presented, in terms of significant height (Figure 6.9). For the **PBr** profile the maximum significant height of the bounded component varies from $0.1m$ (offshore) to $0.2m$ (before the breaking occurs and close to the shore). The free component becomes significant ($H_{sig,free} < 0.1m$) *close to the breaking zone* and in the *surf zone*. For the **PIn** profile, both bound and free components have a constant growth rate through the domain, reaching the maximum value at the inlet ($H_{sig,boun} = 0.15m$ and $H_{sig,free} = 0.2m$).

6.2.3   Reflection analysis

Further analysis includes the separation of the free IG wave to the components (in terms of fluxes):

1. Incoming IG wave
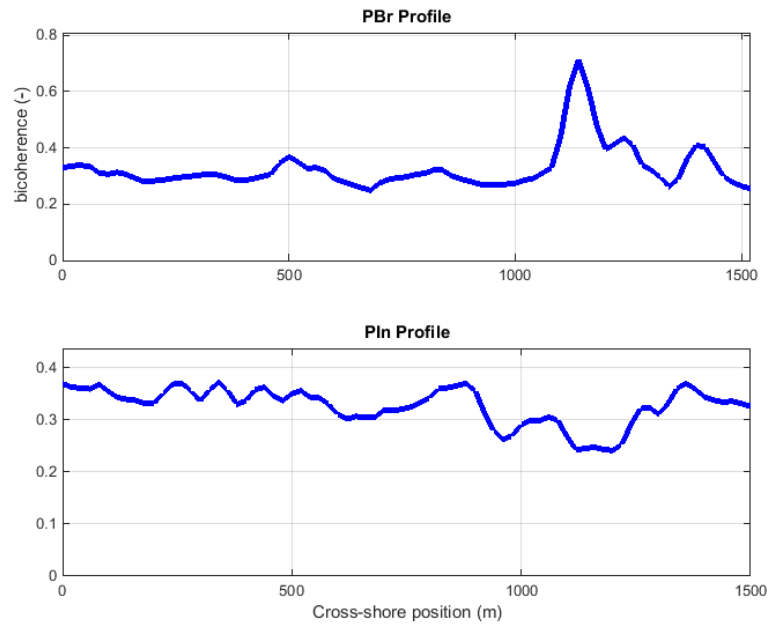
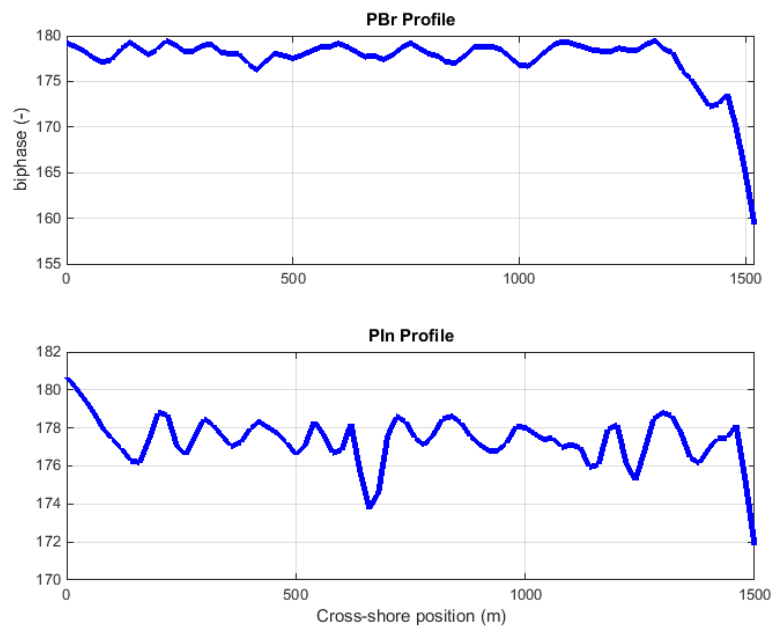FIGURE 6.7: Bicoherence, b, for the **PBr** profile (upper panel) and the **PIn** profile (bottom panel).

FIGURE 6.8: The simulated biphase, θ for the **PBr** profile (upper panel) and the **PIn** profile (bottom panel).
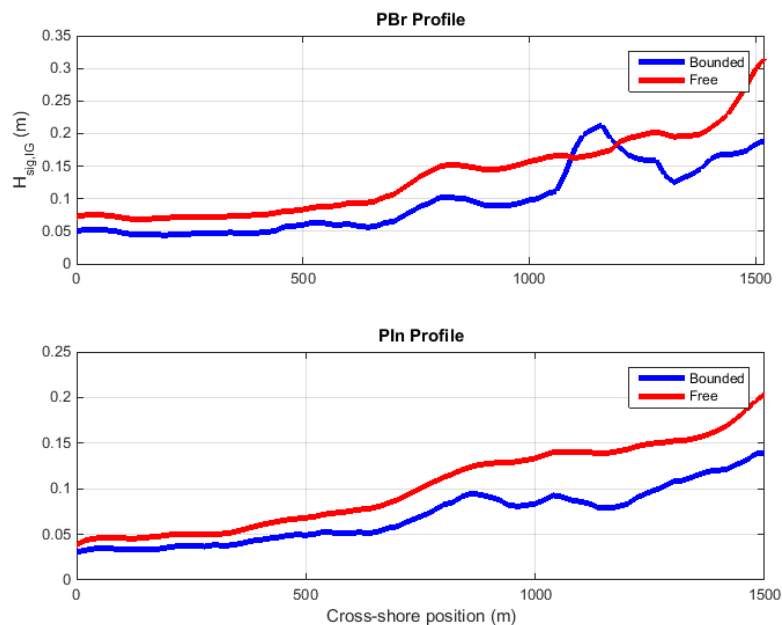
FIGURE 6.9: The significant height, H_{sig}, for the bounded IG (red color) and free IG waves (blue color). Upper panel is the **PBr** profile and the bottom panel the **PIn** profile.

2. Outgoing IG wave

In order to achieve this further decomposition the method of Sheremet et al. [2002] is used (Chapter 2.3). This method requires the local sea-surface elevation and the mean (along-shore and cross-shore) velocity as input. The separation of incoming/outgoing waves is simulated for the **PBr** and **PIn** profile. Finally, fluxes and reflection coefficient are calculated for the IG frequency band $(0.005 - 0.05Hz)$.

Starting with the **PBr** profile, the incoming flux (Figure 6.10, upper left panel) decreases sharply as the IG wave propagates through *the steep slope zone*. Continuing to the *mild slope zone*, the IG flux tends to increase slightly until *the breaking zone*. After the breaking phenomenon, incoming flux drops. The out-coming (reflected) flux follows the same trend as the incoming for *the steep slope zone* but it continues to drop in *the mild slope zone* (until $x = 600m$). Outgoing flux drops between $x = 600m$ and $x = 1000m$ and raises again, entering to *the breaking zone*.

For the **PIn** profile (Figure 6.10, bottom left panel), incoming and outgoing fluxes follow the same declining trend, going from offshore to the location $x = 1100m$ of the entrance channel. At the area between $x = 1100m$ and $x = 1500m$, the incoming flux raises (until $x = 1450m$) and drops close to the harbour inlet. In contrast with the incoming flux, outgoing flux has the opposite trend.
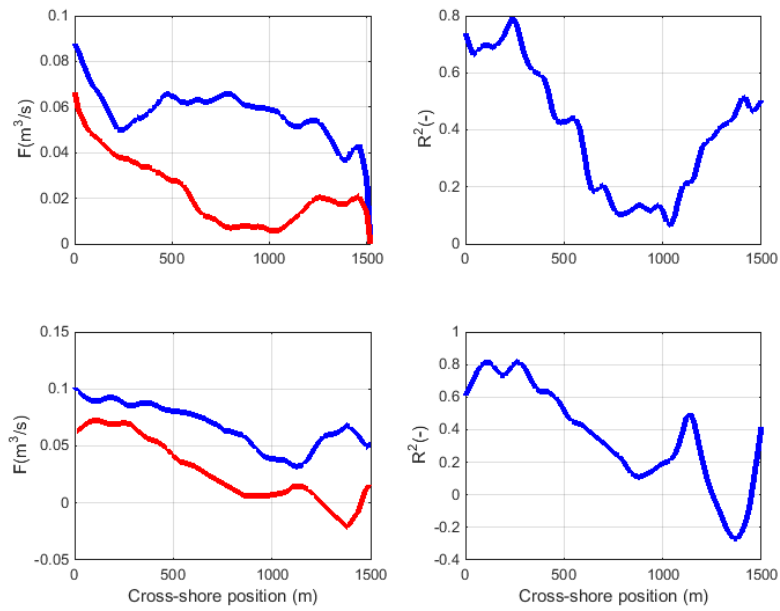
FIGURE 6.10: Left panels: Bulk fluxes, F, for the incoming (blue) and outgoing (red) IG waves. Right panels: Reflection coefficient, R^2 for the IG band. Upper panels are related to the **PBr** profile and bottom panels related to the **PIn** profile.

6.3 Discussion

As it has been mentioned, the decomposition of the wave components is done only for the case of Barbers Point harbour for one wave offshore condition (S16) due to lack of time. In this chapter the results from Chapter 6.2 will be compared with previous studies in order to identify their validity. At the same time, some further conclusions, related with the IG wave behavior in Barbers Point, will be presented. The results are discussed in three different sections:

1. Decomposition of the total signal and the energy transmission

2. The bispectral analysis

3. The reflection analysis

6.3.1 Decomposition of the wave signal and the energy transmission

In order to understand the energy transmission to the sub-harmonics, the offshore wave conditions (S16) have to be examined and the primary-frequency components have to be determined. Offshore wave spectra, S16 (Figure 4.4) is a relatively narrow peaked spectrum and the 95% of its energy is concentrated between frequencies, $f_1 = 0.07Hz$

and $f_2 = 0.11Hz$, and the major part of energy (80%) is located between $f_3 = 0.08Hz$ and $f_4 = 0.10Hz$. As a result, the primar sub-harmonics are expected at frequencies $f_{sub1} = 0.04Hz$ ($f_1 - f_2$) and $f_{sub2} = 0.02Hz$ ($f_3 - f_4$), with the last one to be the most empowered (originated from the interactions of the most empowered short waves). These assumptions (about the frequency location of the sub-harmonics) can be easily confirmed by Figure 6.6 (upper-right panel), where the short waves seem to transfer energy to the IG waves through the frequencies, f_{sub1} and f_{sub2}, at the shoaling area.

Starting from the **PBr** profile, the decomposition of the total signal (Chapter 6.2.1) suggests that the IG waves start to grow after the cross-shore position, $x = 700m$ (Figure 6.5 and Figure 6.3), the starting point of the *mild-slope zone*. The IG waves tend to start to grow at intermediate depths and this result agrees with Rijnsdorp [2011] (and many other researchers). As it was expected, the IG energy is located close to the subharmonic, $f_{sub2} = 0.02Hz$ (Figure 6.3), at the starting point. Moving shorewards, energy seems to be transmitted to other sub-harmonics due to non-linear wave interactions. The results for the spectral evolution (Figure 6.3) is somewhat similar to the patterns that Michallet et al. [2014] described (Figure 2.1).

With regard to the **PIn** profile, IG waves are starting to grow, after the cross-shore position, $x = 1100m$, inside the *entrance channel zone* (Figure 6.4). For this profile, the IG waves originate from areas outside of this profile. At first, the IG waves start to grow after a significant reduce of the short wave energy (Figure 6.4), in deeper waters than to the **PBr** profile. Additionally, the IG wave energy seems to be concentrated in several frequency components, at the starting point, $x = 1100m$. The reduced boundness of the IG waves is caused by reflections (edge and leaky waves) due to the shore and the vertical structures. More about this behavior will be explained in Chapter 6.3.3. Finally, Figure 6.5 shows that the Barbers Point harbour is well protected by the short waves, but not from the IG waves. The IG waves (as long waves) seem to be strongly affected by refraction due to the north edges (Figure 6.1) of the channel, leading to IG propagation into the harbour. On the other hand, short waves (weakly refracted) are following another path to the adjacent shore.

6.3.2 Bispectral analysis

The bispectral analysis (Figure 6.6, upper-right panel) agrees with Henderson et al. [2006], that swell frequencies ($0.08 - 0.11Hz$) transmit energy to their sub-harmonics ($f_{sub1} = 0.4Hz$ and $f_{sub2} = 0.2$). Within the breaking zone , the IG waves start to release due to short wave energy dissipation. As Eldeberky [1996] stated, the IG waves with the lowest frequency are expected to be released first ((Figure 6.6, bottom-left

panel) and the high (in terms of frequency) IG waves are following . Finally, in the swash-zone, a major part of IG waves is released and slight increase of bicoherence is dictating re-generation of bound IG waves in that area (consistent with [Michallet et al., 2014] research).

Bicoherenece and biphase for the **PBr** profile shows similar trend to Ruessink [1998],Eldeberky [1996] (Figure 3.2) and Sheremet et al. [2002]. The IG wave is loosely bounded with the short waves, between $x = 0m$ and $x = 1100m$ (Figure 6.8, upper panel). Reduced coupling (bicoherence) is caused by the leaky IG waves as Eldeberky [1996] presented. Between $x = 1100m$ and $x = 1200m$, short wave- IG wave interactions are amplified as the wave approaches the breaking zone. Inside the breaking zone the complexity of the interpretation increases. The short waves start to break, starting from the short wave components with the highest amount of energy. If the breaking points, for each short wave component, were located at the same position, a sharp decrease of bicoherence would be expected at the breaking point (due to the total release of the IG waves). However, the bicoherence drops significantly (0.7 to 0.4) between $x = 1250m$ and $x = 1300m$, remains constant for $40m$ and decreases again, reaching bicoherence of $b = 0.3$ at $x = 1400m$. The coupling between IG and short waves starts again after the $x = 1400m$ (*surf-zone*). The simulated behavior of IG waves inside the *breaking* and the *surf zone* agrees with the observations of Michallet et al. [2014] and Guedes et al. [2013].

For the **PIn** profile, the interpretation of the IG wave behaviour is relatively simple due to the absence of breaking phenomena (in the transect **PIn**) . Between $x = 0m$ and $x = 900m$, there are no severe fluctuations and bicoherence is similar to the **PBr** profile for this area. However, there is a significant reduction of bicoherence between $x = 1000m$ and $x = 1250m$, and after this zone, bicoherence increases again to $b = 0.34$ until the inlet. The adjacent shore is considered as the origin of the free IG waves at the zone $x = 1000 - 1250$. Another reason of that reduction is the release of IG waves due to refraction, which is explained in Chapter 6.3.1 (last paragraph).

6.3.3 The reflection analysis

Starting from the **PBr** profile (Figure 6.10, upper right panel), IG waves experience a significant reflection ($R^2 = $ 0.2-0.8), but they are not fully reflected ($R^2 = 1$). This means that there is energy dissipation of IG waves due to several mechanisms (Chapter 2.4). However, the reduction of the reflection coefficient in the *surf zone* is not severe [de Bakker et al., 2013] and no IG breaking phenomena are expected. The dominant dissipation mechanism is probably the interaction of the incoming short waves with

the outgoing IG waves, as Thomson et al. [2006] identified (Chapter 2.4). IG energy fluxes for the incoming waves drop significantly compared to those for the out-coming waves, which are remaining relatively constant. The results for the reflection analysis are consistent with the research of Sheremet et al. [2002] and de Bakker et al. [2013] (Figure 2.8).

For the **PIn** profile (Figure 6.10, bottom right panel), the interpretation of the fluxes variations is more complex due to the effect of the adjacent areas and the basin. As mentioned in Chapter 6.3.2, there are evidences that reflected IG waves (from the adjacent areas) are affecting the entrance channel of the Barbers Point harbour, especially between $x = 1000 - 1400$. Edge waves, generated at the shore, are trapped inside the surf-zone and enter to the entrance channel, causing the peak of the reflection coefficient at the location $x = 1200$. Continuing closer to the inlet, the energy of the reflected waves is reduced due to the effect of the harbour. IG waves are reflected from the vertical structures of the basin, but they remain inside the harbour.

Chapter 7

Conclusion

As clarified in Chapter 1, the scope of this thesis is to provide an insight to the IG behavior close harbours. The harbour of Barbers Point in Hawaii has been chosen as a case study. This thesis constitutes one of the first extensive researches related to the simulation and analysis of IG waves in a two-dimensional domain. Here, the answers to the research questions of Chapter 1.4 are summarized and some recommendations for future studies are presented.

7.1   Answering the research questions

In general, IG waves are generated by the interactions of the short waves. Short wave frequency components tend to interact with each other and transmit energy to sub and super harmonics. This energy transmission is amplified as the waves propagates shorewards and the effects of the bottom becomes dominant. IG waves are the generated subharmonics with frequency between 0.005- 0.05 Hz and they are propagating bounded to the short waves (Res. question 1a). After high energy-fluctuations to the short waves, IG waves are released and they propagate freely. Energy variations could occur due to breaking phenomena or reflection (Res. question 1b). After their release, IG waves dissipate because of their interactions with the short waves, IG wave breaking at low-depths or bottom friction. Both free and bound IG waves could induce resonance to the basin, excessive oscillations to the moored vessels and sediment transport close to the harbour inlet (Res. question 1c).

According to literature, there are several types of numerical tools for the IG wave simulation and they can be discretized by their fundamental equations. RANS (Reynolds Averaged Navier Stokes) models are too computational expensive for two-dimensional

cases. On the other hand, Boussinesq models are widely used but they are inaccurate for large depths (for the case of Barbers Point harbour the offshore boundary depth is 50 m). NSWE (Non-linear Shallow Water Equations) models are not so computational intense compared to other type of models. However, due to their equations, NSWE models are incapable of simulating waves at large depths (shallow water equations) and thus calculating the evolution of IG waves (due to the depth integrated shallow water equations (Res. question 2a+2b). SWASH [Zijlema et al., 2011] (NSWE model) overcomes these restrictions. The option of vertical layer separation is implemented to the model (SWASH), making the shallow-water equations accurate even for large depths. Additionally, a non-hydrostatic term is added to the momentum equations, leading to the reintroduction of the vertical flow motion. The product of this phase-resolving model is the surface elevation series and the flow velocities series, along and cross-shore (Res. question 2d). In order to proceed to the IG wave investigation a post-data analysis is needed. FFT (Chapter 3.2) method is used to separate the total wave for different frequency components and then bispectral analysis determines the correlation between these frequency components (Res. question 2c).

Continuing with the set-up of the model, the proper simulation time, for the case of Barbers Point harbour, is considered 75-80 mins. There is a need of 10 mins to arise an equilibrium (for a bi-chromatic case) and approximately 70 mins to achieve a statistically accurate IG wave calculation (simulate more than 100 IG waves) (Res. question 3a). The computational grid is assumed as 3 x 7m, in order to efficiently simulate the short (generation force of IG waves) and the IG waves (Res. question 3b). Off-shore boundary is considered as weakly-reflective, letting the shore reflected waves to escape the domain. However, the same option is not available for the lateral boundaries and sponge layers are used in order to gradually dump the waves at these areas. The reasonable width of 200 m sponge layers is chosen to absorb the energy of the waves (both short and IG) at the lateral boundaries (Res. question 3c). Finally, the vertical structures are considered fully reflective for this thesis project. This assumption leads to inaccuracies to the short wave simulation inside the basin, but it works efficiently for the IG waves (Scope of the thesis) due to the large IG wave length (Res. question 3d).

The model seems to be highly-sensitive to the width of the sponge layers and the grid resolution. For small widths of sponge layers, the reflected waves cause overestimation of the IG wave height. Additionally, a coarse grid resolution leads to the same magnitude (same as the sponge layers) of IG height overestimation (Res. question 3e). As it was expected, the NSWE model, SWASH, is inaccurate for large depths of the offshore region and the use of two vertical layers is suggested. In addition, the NSWE model is slightly sensitive to the location of the breaking zone (defined by the breaking parameter), proving that breaking phenomena have a major effect on the release and not on the

magnitude of the IG wave. After the sensitivity analysis, the IG wave behavior inside the Barbers Point harbour is simulated. The calculated energy spectrums and IG wave heights compared to the measured ones, are presenting consistency and high predictive skill (0.84) (Res. question 3f).

At this point the last step of the set-up is described: the decomposition of the IG wave. In order to separate the free and the bound IG component is used in the area outside of the harbour. Inside the basin, the bispectrum is highly affected by the resonance, leading to overestimations of the bound IG wave part (Res. question 4a). Bispectral analysis showed strong boundness of the IG waves as they approach the breaking zone, gradually IG release in the surf zone and re-generation of bound IG waves in the swash zone. Additionally, IG waves become more loosely bounded when they reach the entrance channel. IG waves tend to leak to the sides of the channel due to the refraction (Res. question 4c). Lastly, reflection analysis showed that IG waves are not fully reflected by the shore (by 60%). Fluctuations of the reflection coefficient (especially inside the surf zone, close and inside the breaking zone) are caused by energy dissipation of the IG wave (Res. question 4d). The mechanism is the interactions of the IG out-going waves with the short incoming waves. There is no evidence of IG wave breaking and the bottom friction is considered as a minor dissipation mechanism [Rijnsdorp et al., 2014] (Chapter 2.4) due to the mild reflectivity of the shore.

7.2 Recommendations

It is valuable to get more inside into the IG wave behavior. Therefore, it is recommended to apply the post-analysis (bispectral and reflection) for more offshore wave conditions and different harbour cases (i.e steeper slopes). The aim is to determine the consistency of the bispectral and reflection analysis [Sheremet et al., 2002] as decomposition tools.

Another recommendation is the development of a decomposition method which is applicable inside the basin, where resonance occurs. This method would lead to the quantification of IG wave release due to diffraction inside the harbour. IG wave release due to the phenomenon of diffraction has been studied only in theoretical level by Zhou and Liu [1987].

Another recommendation is the further separation of the outgoing IG wave to the leaky and edge component. A method has to be defined which decomposes the different modes of the trapped IG waves inside the surf-zone (Chapter 2.3). Unfortunately, in this case the width of the simulated domain is not sufficient for accurate edge wave simulation.

From an engineering point of view, the identification of IG wave mitigation measures is interesting. There are no direct measures to avoid the presence of IG waves inside the basin due to their large wave-length. However, adjustments to the bathymetry (especially of the entrance channel) would affect the refraction of the longer components, relocating the propagation direction of the IG waves at the adjacent shores. Additionally, the breakwaters inside the surf-zone and parallel to the shoreline would lead to the relocation of the edge waves [Chen et al., 2004a].

With regard to the numerical model,SWASH, a better representation of the boundaries is suggested. Spatial variation of the wave conditions at the offshore boundaries would lead to more accurate simulations. Additionally, the option of weakly reflective lateral boundaries would avoid the existence of reflective waves (on the lateral boundaries) inside the domain. Finally, the vertical discretization of the porosity would be helpful for a better representation of the harbour structures.

Appendix A

Background knowledge

A.1 Hilbert transformation

The boundness of the IG wave is related to the variation of the wave amplitude. In general, the wave envelope quantifies these amplitude fluctuations. Hilbert transformation is applied in order to obtain the wave envelope for the short waves. The short wave surface elevation signal is decomposed by the total (by using FFT method) and the Hilbert transformation function of MATLAB is used on that signal. Continuing, the frequency limits of the wave envelope have to correspond with the IG wave frequency limits (0.005-0.05Hz) for this thesis project. The wave envelope is calculated by using Eq. A.1 [Janssen et al., 2003]:

$$|\alpha(t)| = |\zeta^{sw}(t) + i\gamma^{sw}(t)|^{IG} \tag{A.1}$$

where t is the time, γ is the Hibert operator, ζ^{sw} the surface elevation for the short waves and α the envelope of the surface elevation. Finally, IG superscript denotes the IG frequency restrictions.

A.2 Cross-correlation

Cross-Correlation (also called cross-covariance) between two input signals is a kind of template matching. Cross-correlation can be done in any number of dimensions. The one-dimensional normalized cross-correlation between two input signals is defined as:

$$r(d) = \frac{\sum \left((x(i) - mx) * (y(i - d) - my) \right)}{\sqrt{\sum \left(x(i) - mx \right)^2} \sqrt{\sum \left(y(i - d) - my \right)^2}} \tag{A.2}$$

The coefficient,r, is a measurement of the size and direction of the linear relationship between variables x and y (d is the time lag and mx and my are the mean values of the x and y series respectively). If these variables move together, where they both rise at an identical rate, then r= +1. If the other variable does not budge, then r= 0. If the other variable falls at an identical rate, then r= -1. If r is greater than zero, we have positive correlation. If r is less than zero, we have negative correlation.

A.3 Breaking criterion

Weggel [1972] developed an equation for the breaker depth index from previous laboratory data collected on slopes of 1/5,1/10,1/15,1/20, and1/50.The resulting relationship is expressed as:

$$\frac{H_b}{d_b} = b_m - a_m \frac{H_b}{gT^2} \tag{A.3}$$

where T is the wave period, H_b is the significant height at the breaking point and d_b the depth when breaking occurs. The parameters a_m and b_m are empirically determined functions of beach slope (m), given by:

$$a_m = 43.8(1 - e^{19m}) \tag{A.4}$$

$$b_m = \frac{1.56}{1 + e^{-19.5m}} \tag{A.5}$$

Appendix B

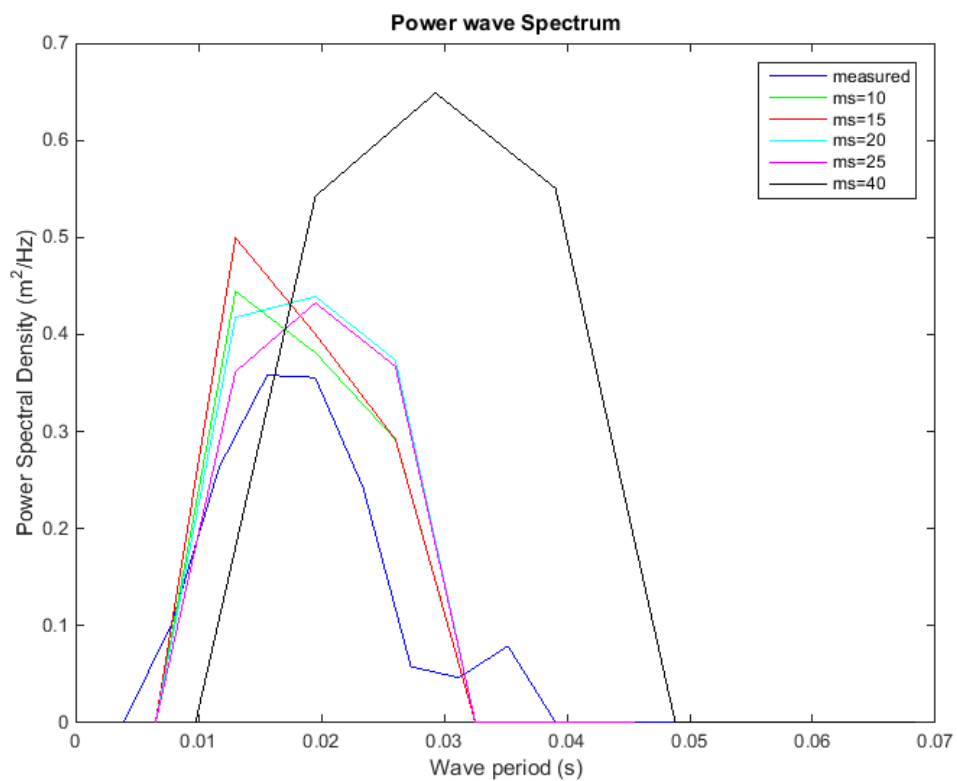# Sensitivity analysis and results for the S17 storm

FIGURE B.1: The IG wave energy spectrum for S17 and for different values of directional spreading at the location 059-P1. Blue is the measured form CDIP, green for m_s=10, red for m_s=15, cyan for m_s=20, magenta for m_s=25 and yellow for m_s=40.

TABLE B.1: The IG wave significant height for different directional spreading values compared to the observed one (S17 and buoy 059-P1).

Directional spreading, m_s	Significant IG wave height, $H_{IG,sig}$ (m)
Observed	0.40
10	0.36
15	0.37
20	0.37
25	0.39
40	0.46
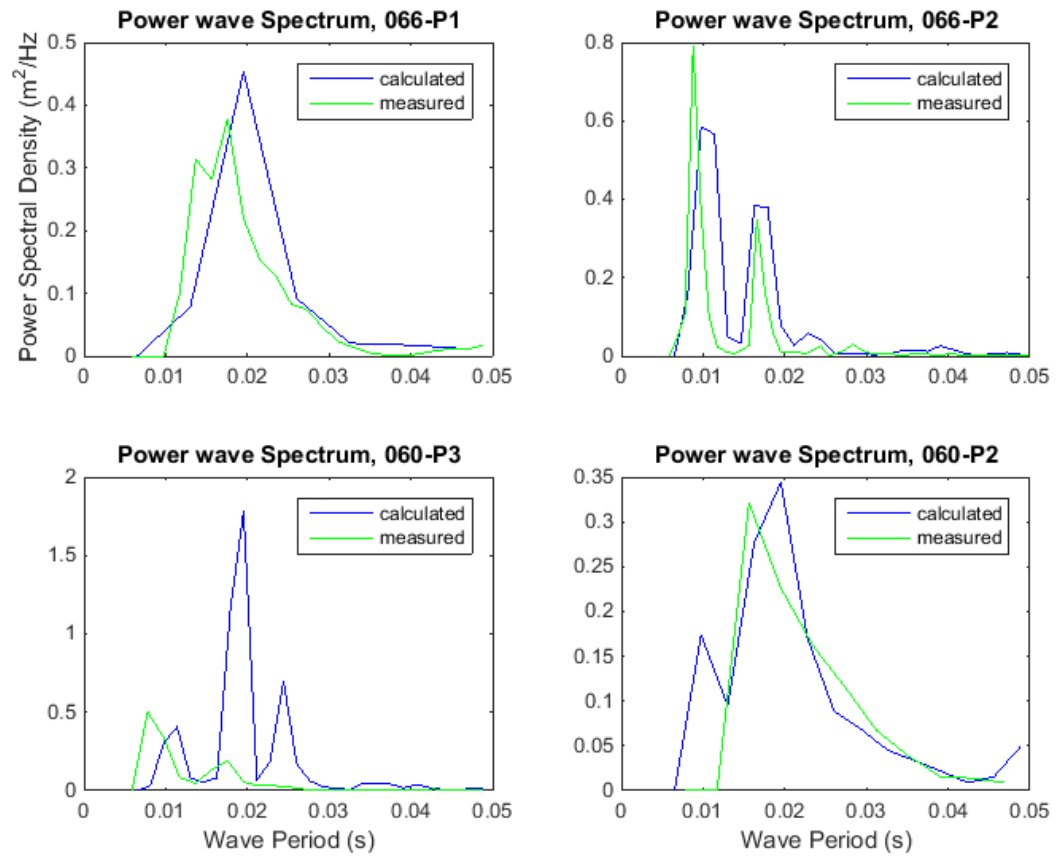
FIGURE B.2: Energy spectrums calculated for S17 at different locations, 066-P1,066-P2,066-P3 and 060-P2 compared with the measured spectrums by CDIP.

TABLE B.2: The IG wave significant height for different locations inside the basin compared with the measured ones (S17).

Buoy	Observed $H_{sig,IG}$ (m)	Calculated, $H_{sig,IG}$ (m)
066-P1	0.32	0.34
066-P2	0.30	0.31
060-P3	0.28	0.44
066-P2	0.29	0.31

Appendix C

Amplification factors for the Barbers Point harbour

The amplification factor is the ratio between the energy at several gauges inside the basin and the energy outside of the basin and close to the inlet. Outside of the Barbers Point harbour, at the buoy 059-P1, the IG waves are considered fully developed. Amplification of the low-frequency energy inside the basin is considered as an effect of the resonance. So, low-frequency components with amplification factor higher than 1 are considered as one of the basin;'s natural frequency.
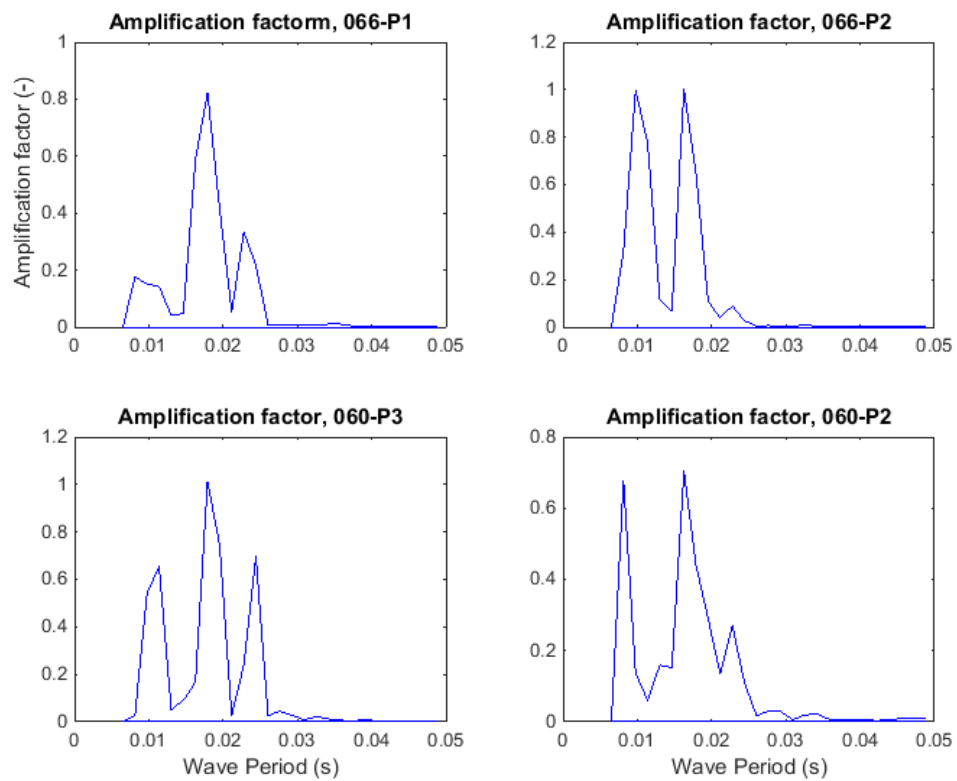
FIGURE C.1: Amplification factor for different locations inside the basin (066-P1,066-P2,066-P3 and 060-P2) for the S16.
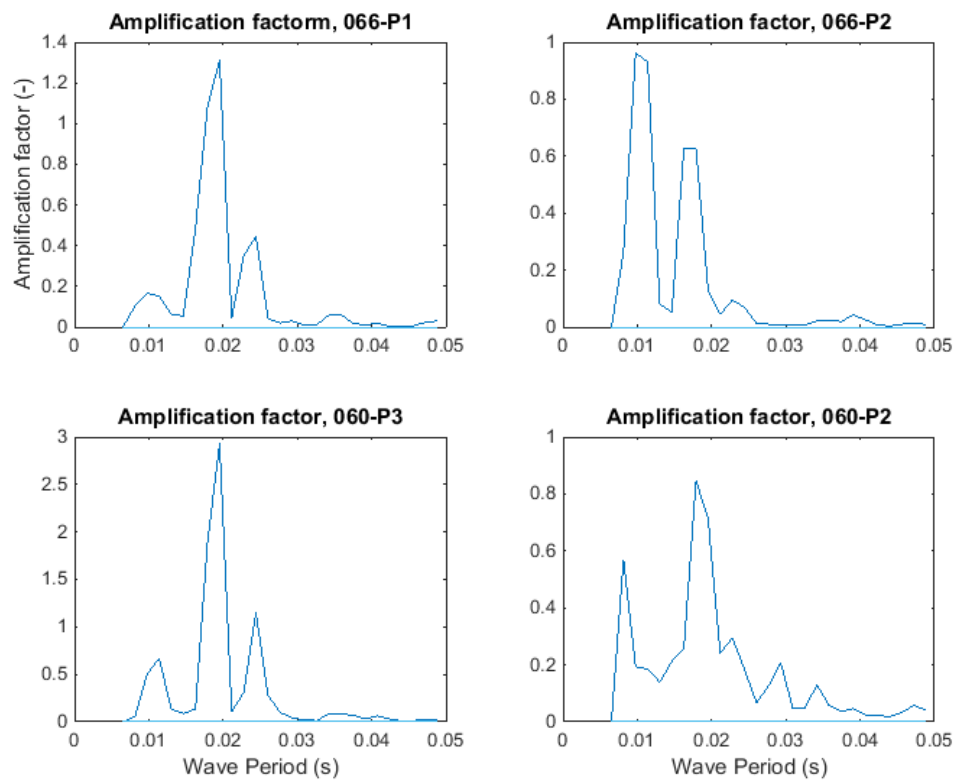
FIGURE C.2: Amplification factor for different locations inside the basin (066-P1,066-P2,066-P3 and 060-P2) for the S17.

Appendix D

Breaking Zones
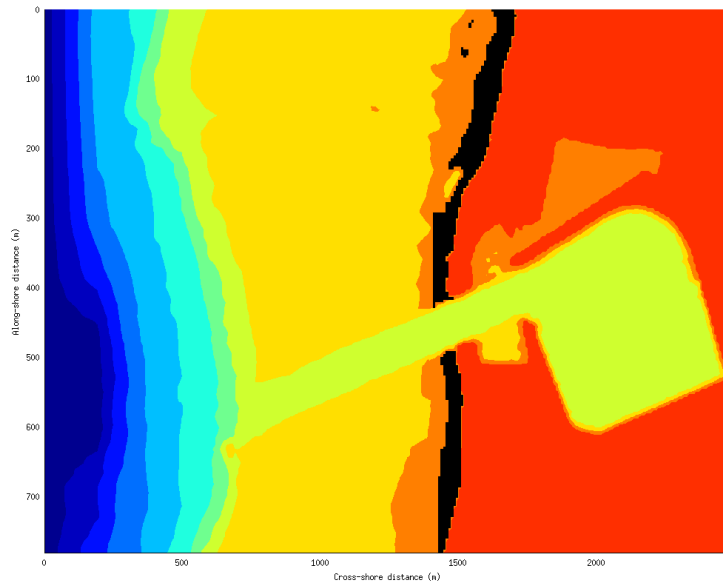
FIGURE D.1: The breaking zones (black) for the simulated wave condition S16 according to the SWASH bore concept.
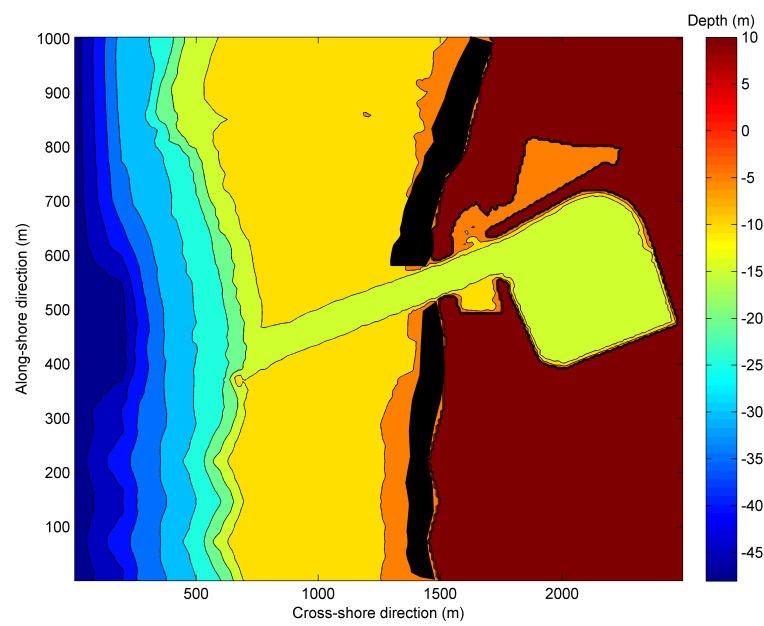
FIGURE D.2: The breaking zones (black) for the simulated wave condition S16 according to the Weggel [1972] breaking criterion.

Appendix E

Directional spectra

The directional spectrums are calculated by using MATLAB. The surface elevation, ζ, and the velocities alongshore (u_y) and cross-shore (u_x) are used in order to calculate the energy magnitude and the propagation direction of the wave. Waves are separated to IG and short waves and the directional spectrums for different locations (both profiles, **PBr** and **PIn**) are presented. Finally, the offshore boundary is located at the 90° degrees and the Barbers point harbor at the 270° degrees.
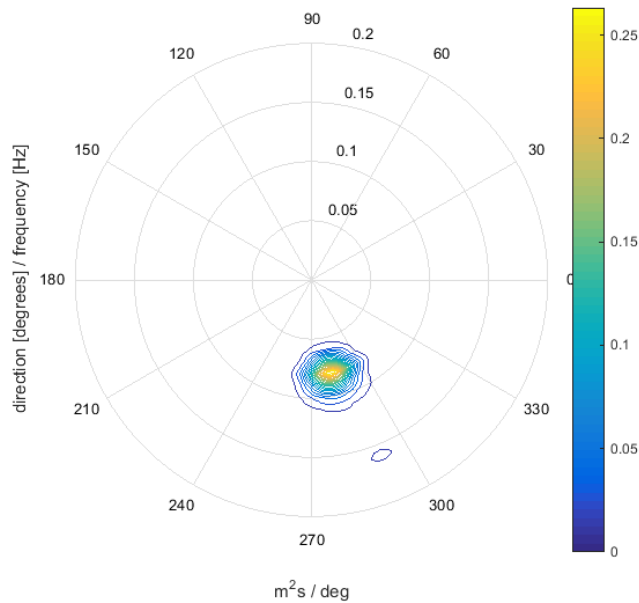
FIGURE E.1: Directional spectrum for the short waves at the location, $x = 200m$ (Profile **PBr**).
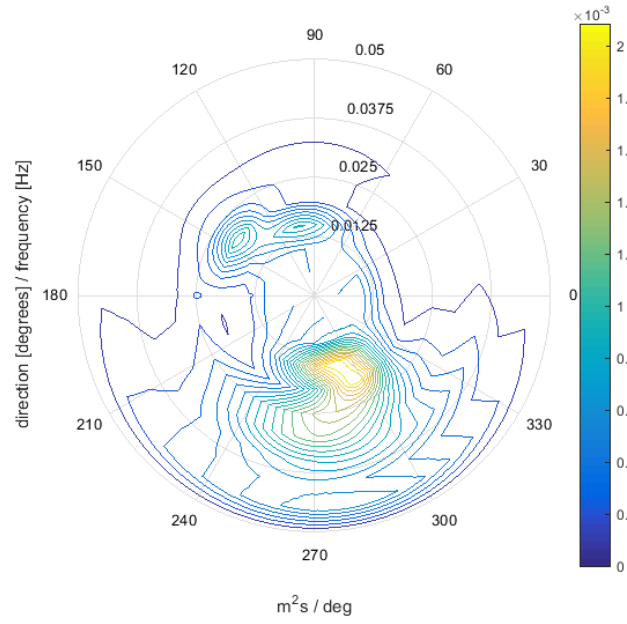
FIGURE E.2: Directional spectrum for the IG waves at the location, $x = 200m$ (Profile **PBr**).
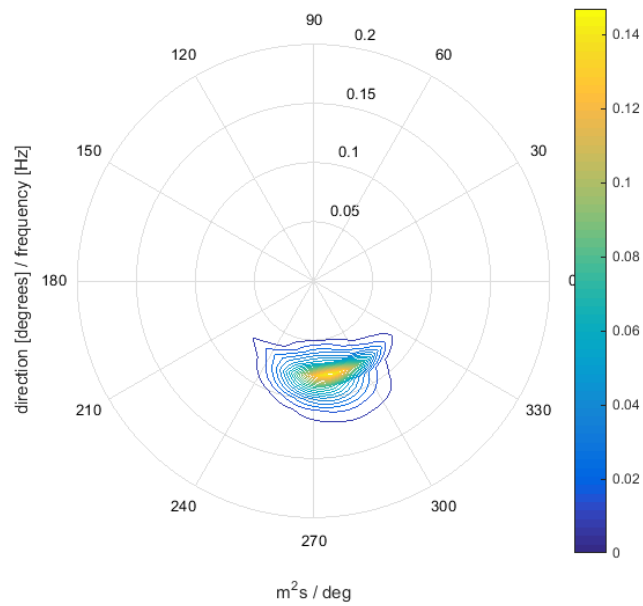

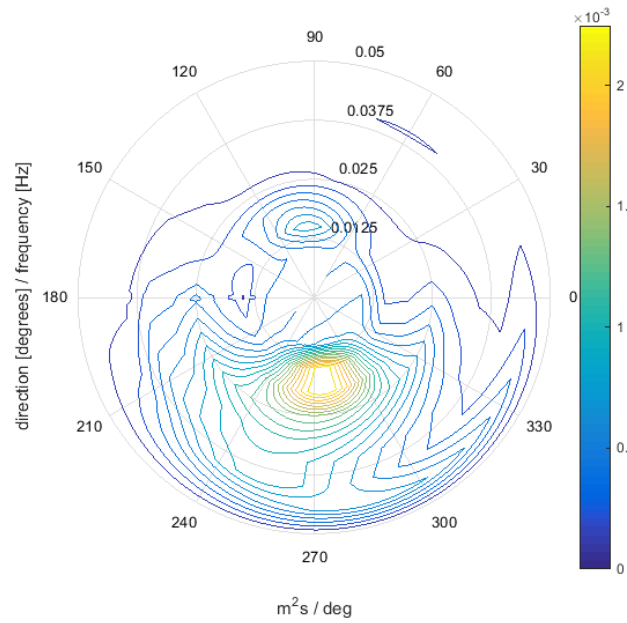FIGURE E.3: Directional spectrum for the short waves at the location, $x = 500m$ (Profile **PBr**).

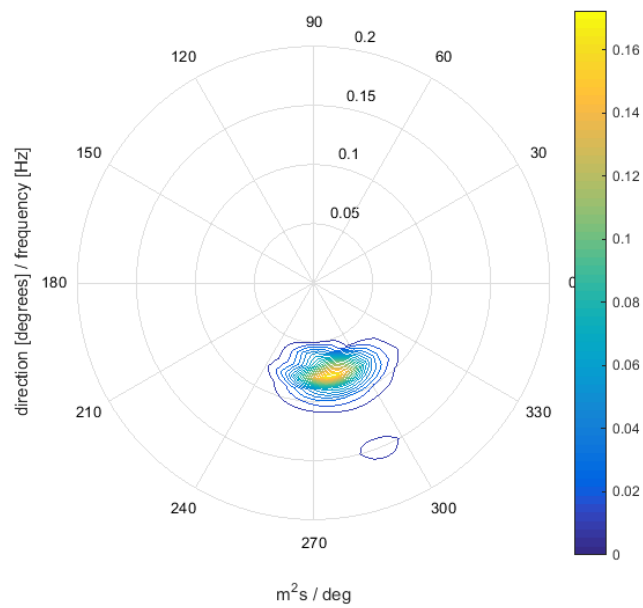FIGURE E.4: Directional spectrum for the IG waves at the location, $x = 500m$ (Profile **PBr**).

FIGURE E.5: Directional spectrum for the short waves at the location, $x = 1200m$ (Profile **PBr**).
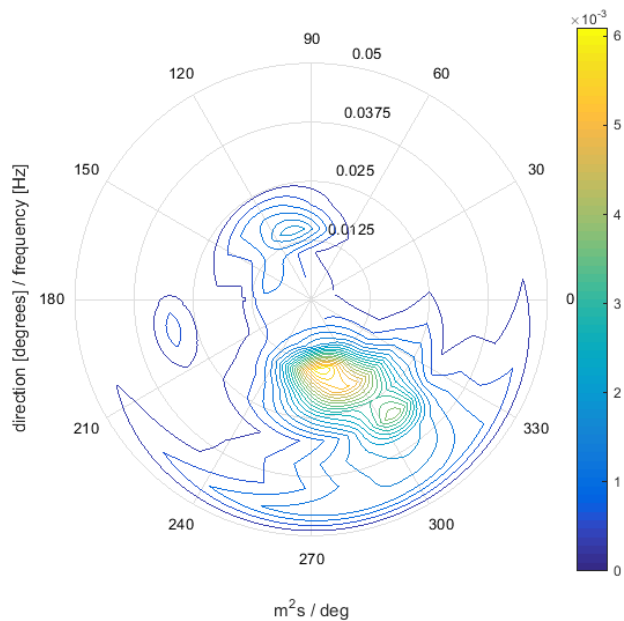
FIGURE E.6: Directional spectrum for the IG waves at the location, $x = 1200m$ (Profile **PBr**).
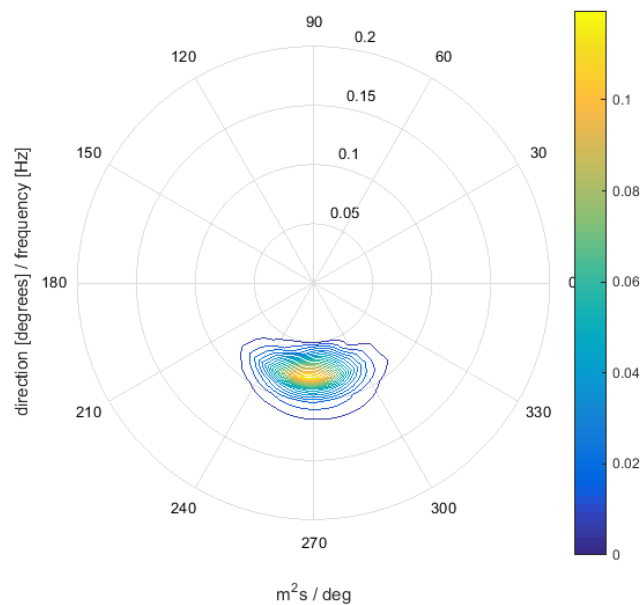

FIGURE E.7: Directional spectrum for the short waves at the location, $x = 1460m$ (Profile **PBr**).
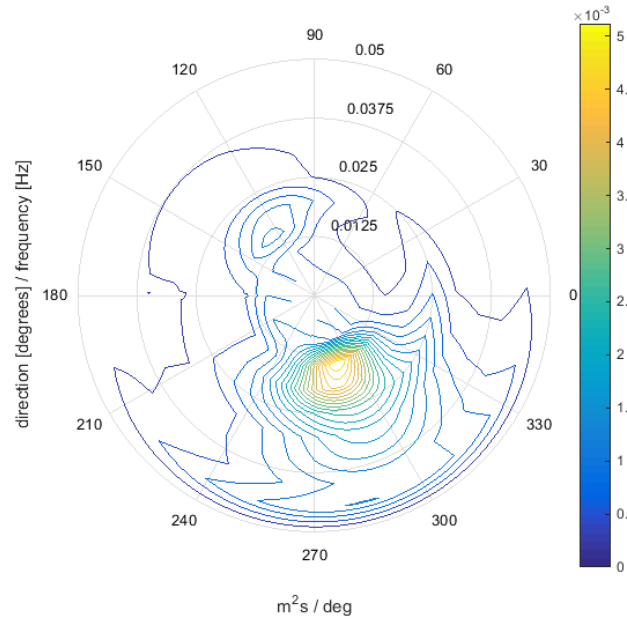
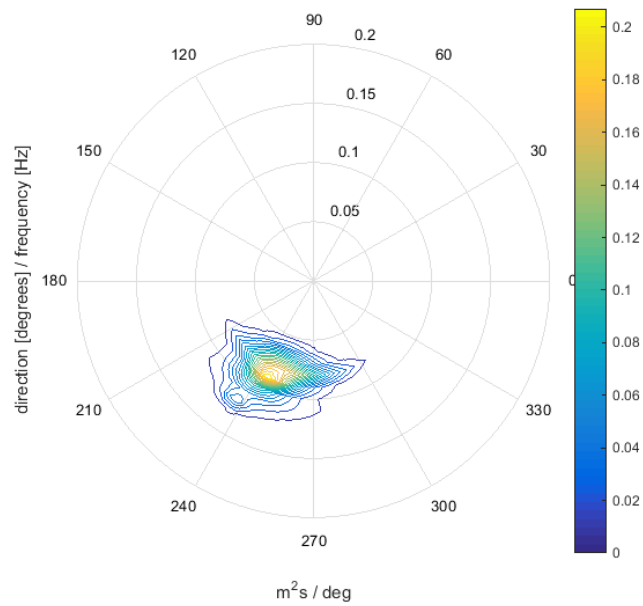FIGURE E.8: Directional spectrum for the IG waves at the location, $x = 1460m$ (Profile **PBr**).

FIGURE E.9: Directional spectrum for the short waves at the location, $x = 200m$ (Profile **PIn**).
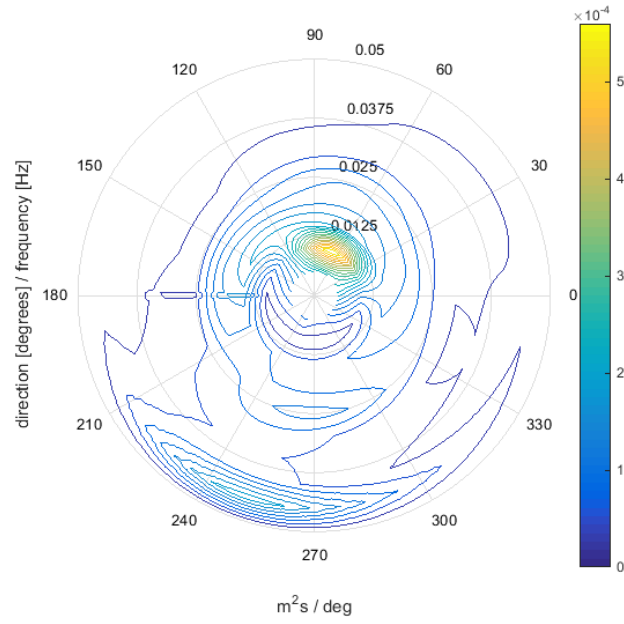
FIGURE E.10: Directional spectrum for the IG waves at the location, $x = 200m$ (Profile **PIn**).

FIGURE E.11: Directional spectrum for the short waves at the location, $x = 500m$ (Profile **PIn**).

FIGURE E.12: Directional spectrum for the IG waves at the location, $x = 500m$ (Profile **PIn**).

FIGURE E.13: Directional spectrum for the short waves at the location, $x = 1200m$ (Profile **PIn**).
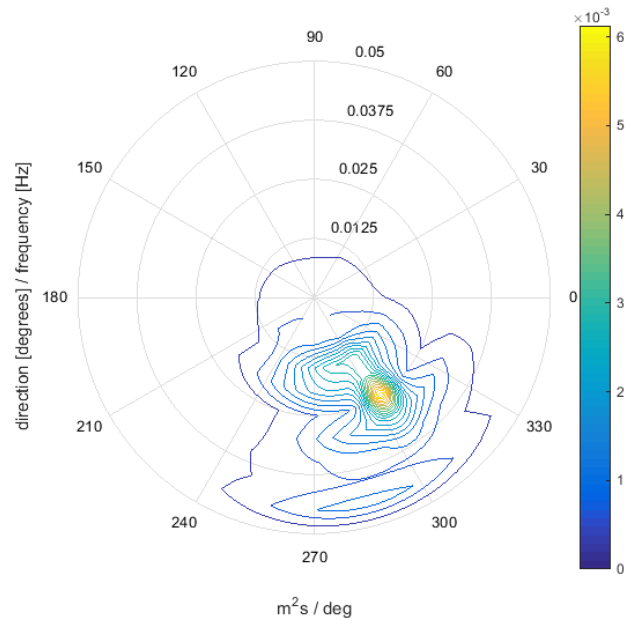
FIGURE E.14: Directional spectrum for the IG waves at the location, $x = 1200m$ (Profile **PIn**).
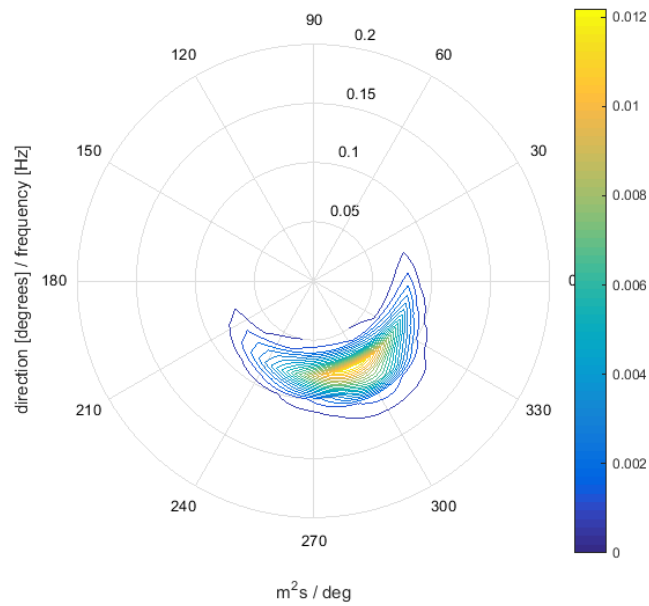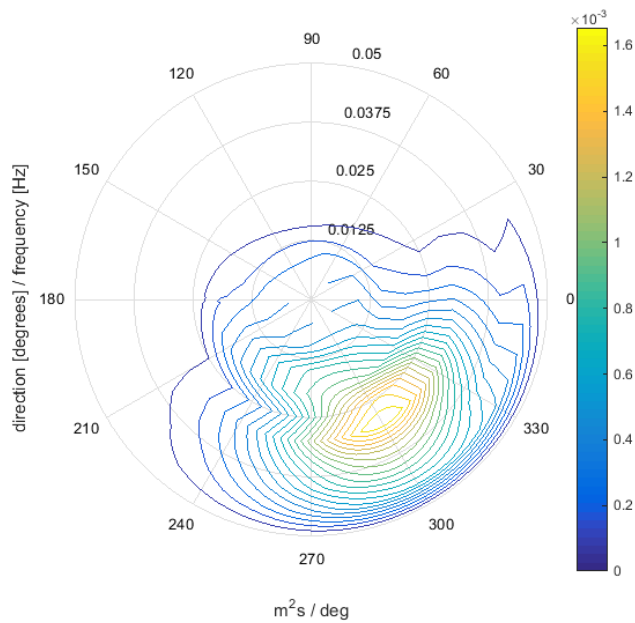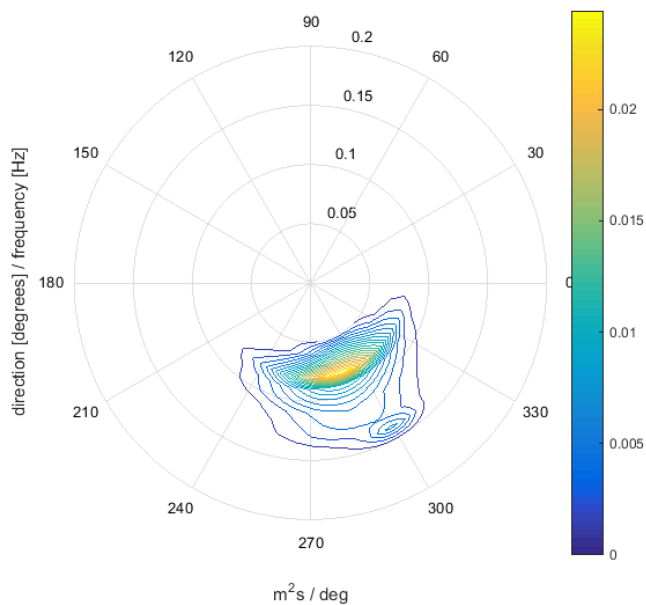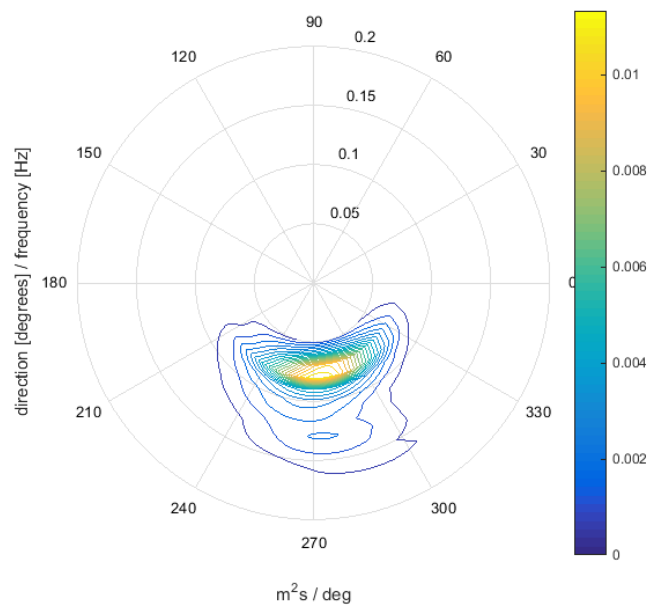

FIGURE E.15: Directional spectrum for the short waves at the location, $x = 1460m$ (Profile **PIn**).
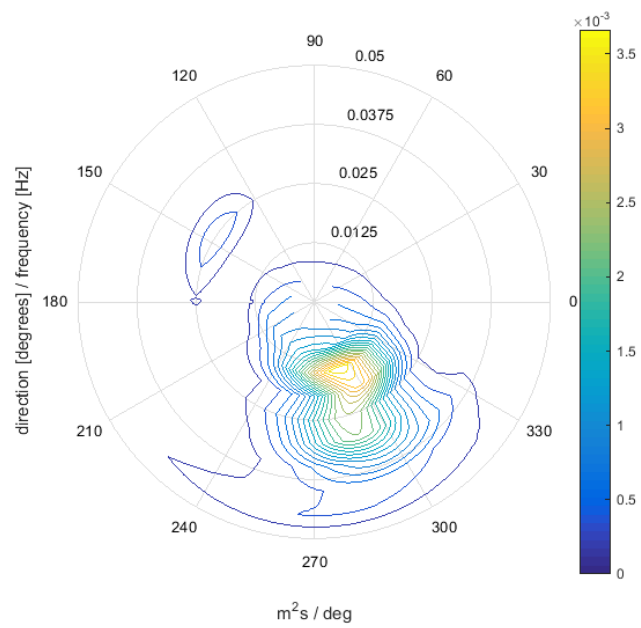
FIGURE E.16: Directional spectrum for the IG waves at the location, $x = 1460m$ (Profile **PIn**).

Appendix F

Bispectra analysis for the PIn profile

FIGURE F.1: Normalized bispectrum (bicoherence) at the location $x = 200m$ for the **PIn** profile.

FIGURE F.2: Normalized bispectrum (bicoherence) at the location $x = 500m$ for the **PIn** profile.

FIGURE F.3: Normalized bispectrum (bicoherence) at the location $x = 1200m$ for the **PIn** profile.

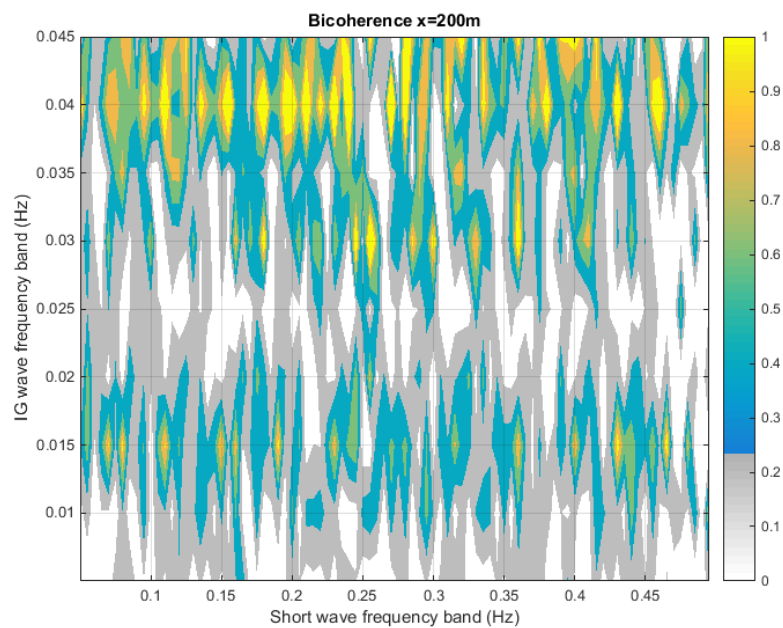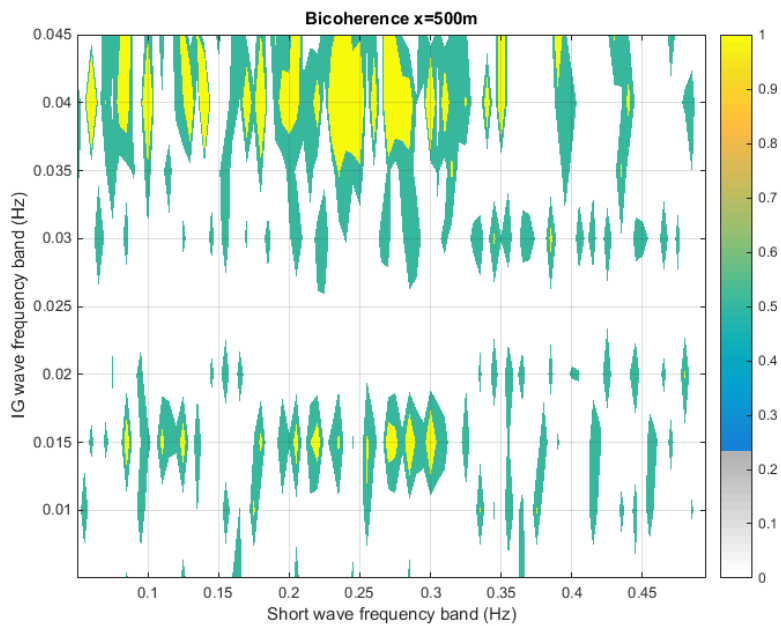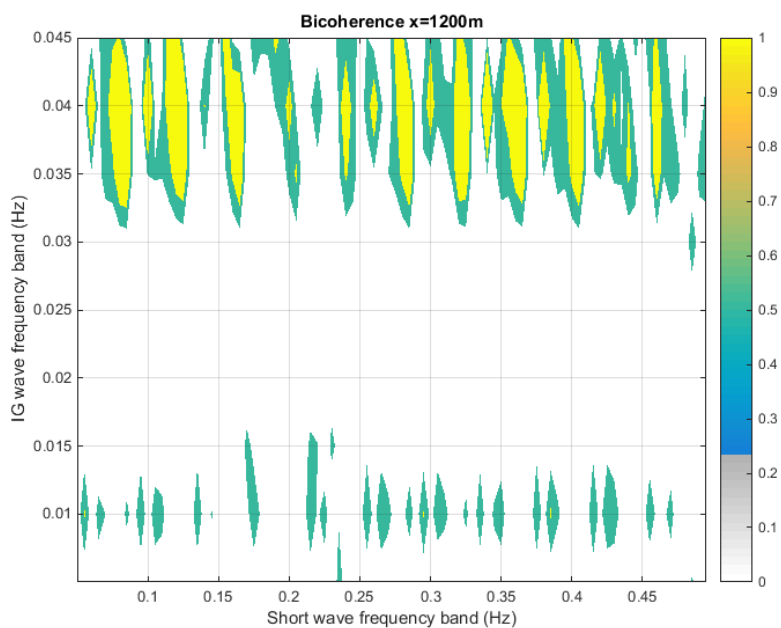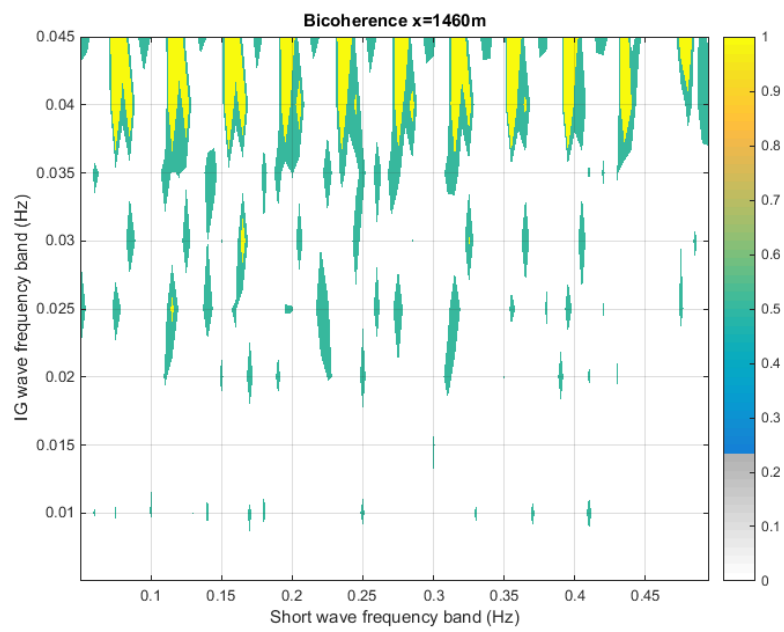FIGURE F.4: Normalized bispectrum (bicoherence) at the location $x = 1460m$ for the **PIn** profile.

Bibliography

A Sheremet, RT Guza, Steve Elgar, and THC Herbers. Observations of nearshore infragravity waves: Seaward and shoreward propagating components. *Journal of Geophysical Research: Oceans (1978–2012)*, 107(C8):10–1, 2002.

Walter Munk. Origin and generation of waves. *Coastal Engineering Proceedings*, 1(1), 1950. ISSN 2156-1028. URL https://icce-ojs-tamu.tdl.org/icce/index.php/icce/article/view/904.

Hervé Michallet, Gerben Ruessink, Mariana VL Rocha, Anouk De Bakker, Dominic Van Der A, Andrea Ruju, Paulo A Silva, Nadia Sénéchal, Vincent Marieu, Marion Tissier, et al. Globex: Wave dynamics on a shallow sloping beach. In *HYDRALAB IV Joint User Meeting, Lisbon, July 2014*, 2014.

THC Herbers, Steve Elgar, RT Guza, and WC O'Reilly. Infragravity-frequency (0.005-0.05 hz) motions on the shelf. part ii: Free waves. *Journal of physical oceanography*, 25(6):1063–1079, 1995.

Michael S Longuet-Higgins and R_W Stewart. Radiation stress and mass transport in gravity waves, with application to 'surf beats'. *Journal of Fluid Mechanics*, 13(04): 481–504, 1962.

JA Battjes, HJ Bakkenes, TT Janssen, and AR Van Dongeren. Shoaling of subharmonic gravity waves. *Journal of Geophysical Research: Oceans (1978–2012)*, 109(C2), 2004.

Peter J McComb, David L Johnson, and Brett J Beamsley. Numerical study of options to reduce swell and long wave penetration at port geraldton. *Coasts and Ports 2009: In a Dynamic Environment*, page 490, 2009.

KT Holland and Robert A Holman. Wavenumber-frequency structure of infragravity swash motions. *Journal of Geophysical Research: Oceans (1978–2012)*, 104(C6): 13479–13488, 1999.

IK Van Giffen. Long wave case study for barbers point harbour, hawaii. 2003.

Anouk de Bakker, Marion Tissier, Vincent Marieu, Nadia Sénéchal, Andrea Ruju, Javier Lara, and BG Ruessink. Infragravity wave propagation and dissipation on a low-sloping laboratory beach. In *Proceedings of the Conference on Coastal Dynamics*, 2013.

Yasser Eldeberky. *Nonlinear transformation of wave spectra in the nearshore*. TU Delft, Delft University of Technology, 1996.

Mark Buckley, Ryan Lowe, and Jeff Hansen. Evaluation of nearshore wave models in steep reef environments. *Ocean Dynamics*, 64(6):847–862, 2014.

Richard J Weggel. Maximum breaker height. *" Journal of the Waterways, Harbors and Coastal Engineering Division*, 98(4):529–548, 1972.

THC Herbers and MC Burton. Nonlinear shoaling of directionally spread waves on a beach. *Journal of Geophysical Research: Oceans (1978–2012)*, 102(C9):21101–21114, 1997.

Spahr C Webb, Xin Zhang, and Wayne Crawford. Infragravity waves in the deep ocean. *Journal of Geophysical Research: Oceans (1978–2012)*, 96(C2):2723–2736, 1991.

RT Guza and Edward B Thornton. Observations of surf beat. *Journal of Geophysical Research: Oceans (1978–2012)*, 90(C2):3161–3172, 1985.

Guan-Yu Chen, Chung-Ching Chien, Ching-Ho Su, and Hsiang-Mao Tseng. Resonance induced by edge waves in hua-lien harbor. *Journal of oceanography*, 60(6):1035–1043, 2004a.

Wim Van Der Molen, Patricio Monardez, and Ap Van Dongeren. Numerical simulation of long-period waves and ship motions in tomakomai port, japan. *Coastal Engineering Journal*, 48(01):59–79, 2006.

Reginald A Beach and Richard W Sternberg. Suspended sediment transport in the surf zone: response to cross-shore infragravity motion. *Marine Geology*, 80(1):61–79, 1988.

Vincent Leys and Ryan P Mulligan. Modelling coastal sediment transport for harbour planning: selected case studies. *Sediment Transport, http://www. intechopen. com/articles/show/title/modelling-coastal-sediment-transport-forharbour-planning-selected-case-studies*, 2011.

Okey Nwogu and Zeki Demirbilek. Infragravity wave motions and runup over shallow fringing reefs. *Journal of waterway, port, coastal, and ocean engineering*, 136(6):295–305, 2010.

Marcel Zijlema, Guus Stelling, and Pieter Smit. Swash: An operational public domain code for simulating wave fields and rapidly varied flows in coastal waters. *Coastal Engineering*, 58(10):992–1012, 2011.

Dano Roelvink, Ad Reniers, AP van Dongeren, Jaap van Thiel de Vries, Robert McCall, and Jamie Lescinski. Modelling storm impacts on beaches, dunes and barrier islands. *Coastal Engineering*, 56(11):1133–1152, 2009.

Dirk Pieter Rijnsdorp, Pieter Bart Smit, and Marcel Zijlema. Non-hydrostatic modelling of infragravity waves using swash. *Coastal Engineering Proceedings*, 1(33):currents–27, 2012.

Costas Emmanuel Synolakis. Green's law and the evolution of solitary waves. *Physics of Fluids A: Fluid Dynamics (1989-1993)*, 3(3):490–491, 1991.

Eizo Nakaza and Mikio Hino. Bore-like surf beat in a reef zone caused by wave groups of incident short period waves. *Fluid Dynamics Research*, 7(2):89, 1991.

Graham Symonds, David A Huntley, and Anthony J Bowen. Two-dimensional surf beat: Long wave generation by a time-varying breakpoint. *Journal of Geophysical Research: Oceans (1978–2012)*, 87(C1):492–498, 1982.

Guohai Dong, Xiaozhou Ma, Jianwu Xu, Yuxiang Ma, and Gang Wang. Experimental study of the transformation of bound long waves over a mild slope with ambient currents. *Coastal Engineering*, 56(10):1035–1042, 2009.

CHINPU Zhou and PHILIP L-F Liu. Second-order low-frequency wave forces on a vertical circular cylinder. *Journal of Fluid Mechanics*, 175:143–156, 1987.

MW McBride, JV Smallman, and NWH Allsop. Guidelines for the hydraulic design of harbour entrances. 1996.

Gordon S Harkins and Michael J Briggs. Resonant forcing of harbors by infragravity waves. *Coastal Engineering Proceedings*, 1(24), 1994.

F Ursell. Edge waves on a sloping beach. *Proceedings of the royal society of London. Series A. Mathematical and Physical Sciences*, 214(1116):79–97, 1952.

EC Bowers. Harbour resonance due to set-down beneath wave groups. *Journal of Fluid Mechanics*, 79(01):71–92, 1977.

Y Ciriano, A Falqués, and MA Losada. Resonance of a harbour under edge waves forcing. In *Coastal Engineering 2000*, pages 3580–3591. ASCE, 2001.

Guan-Yu Chen, Chung-Ching Chien, Ching-Ho Su, and Hsiang-Mao Tseng. Resonance induced by edge waves in hua-lien harbor. *Journal of oceanography*, 60(6):1035–1043, 2004b.

Jim Thomson, Steve Elgar, Britt Raubenheimer, THC Herbers, and RT Guza. Tidal modulation of infragravity waves via nonlinear energy losses in the surfzone. *Geophysical Research Letters*, 33(5), 2006.

A Van Dongeren, J Battjes, T Janssen, J Van Noorloos, K Steenhauer, G Steenbergen, and AJHM Reniers. Shoaling and shoreline dissipation of low-frequency waves. *Journal of Geophysical Research: Oceans (1978–2012)*, 112(C2), 2007.

Stephen M Henderson and AJ Bowen. Observations of surf beat forcing and dissipation. *Journal of Geophysical Research: Oceans (1978–2012)*, 107(C11):14–1, 2002.

Stephen M Henderson, RT Guza, Steve Elgar, THC Herbers, and AJ Bowen. Nonlinear generation and loss of infragravity wave energy. *Journal of Geophysical Research: Oceans (1978–2012)*, 111(C12), 2006.

Dirk P Rijnsdorp, Pieter B Smit, and Marcel Zijlema. Non-hydrostatic modelling of infragravity waves under laboratory conditions. *Coastal Engineering*, 85:30–42, 2014.

Jaak Monbaliu, Roberto Padilla-Hernandez, Julia C Hargreaves, Juan Carlos Carretero Albiach, Weimin Luo, Mauro Sclavo, and Heinz Guenther. The spectral wave model, wam, adapted for applications with high spatial resolution. *Coastal engineering*, 41 (1):41–62, 2000.

Philippe Bonneton, Florent Chazel, David Lannes, Fabien Marche, and Marion Tissier. A splitting approach for the fully nonlinear and weakly dispersive green–naghdi model. *Journal of Computational Physics*, 230(4):1479–1498, 2011.

Mara Tonelli and Marco Petti. Shock-capturing boussinesq model for irregular wave propagation. *Coastal Engineering*, 61:8–19, 2012.

M Tissier, P Bonneton, F Marche, F Chazel, and D Lannes. A new approach to handle wave breaking in fully non-linear boussinesq models. *Coastal Engineering*, 67:54–66, 2012.

Per A Madsen, OR Sørensen, and HA Schäffer. Surf zone dynamics simulated by a boussinesq type model. part ii: Surf beat and swash oscillations for wave groups and irregular waves. *Coastal Engineering*, 32(4):289–319, 1997.

Pieter Smit, Marcel Zijlema, and Guus Stelling. Depth-induced wave breaking in a non-hydrostatic, near-shore wave model. *Coastal Engineering*, 76:1–16, 2013.

Gangfeng Ma, Fengyan Shi, and James T Kirby. Shock-capturing non-hydrostatic model for fully dispersive surface wave processes. *Ocean Modelling*, 43:22–35, 2012.

JL Lara, IJ Losada, and R Guanche. Wave interaction with low-mound breakwaters using a rans model. *Ocean engineering*, 35(13):1388–1400, 2008.

Tomohiro Suzuki, Toon Verwaest, William Veale, Koen Trouw, and Marcel Zijlema. A numerical study on the effect of beach nourishment on wave overtopping in shallow foreshores. *Coastal Engineering Proceedings*, 1(33):waves–50, 2012.

Changhoon Lee, Woo Sun Park, Yong-Sik Cho, and Kyung Doug Suh. Hyperbolic mild-slope equations extended to account for rapidly varying topography. *Coastal Engineering*, 34(3):243–257, 1998.

G Stelling and M Zijlema. An accurate and efficient finite-difference algorithm for non-hydrostatic free-surface flow with application to wave propagation. *International Journal for Numerical Methods in Fluids*, 43(1):1–23, 2003.

DCL Lam and RB Simpson. Centered differencing and the box scheme for diffusion convection problems. *Journal of Computational Physics*, 22(4):486–500, 1976.

Eric Blayo and Laurent Debreu. Revisiting open boundary conditions from the point of view of characteristic variables. *Ocean modelling*, 9(3):231–252, 2005.

JK Kostense. Measurements of surf beat and set-down beneath wave groups. *Coastal Engineering Proceedings*, 1(19), 1984.

Yuxiang Ma, Guohai Dong, and Xiaozhou Ma. Separation of low-frequency waves by an analytical method. *Coastal Engineering Proceedings*, 1(32):waves–64, 2011.

Klaus Hasselmann, Walter Munk, and Gordon MacDonald. Bispectra of ocean waves. *Time Series Analysis*, pages 125–139, 1963.

BG Ruessink. Bound and free infragravity waves in the nearshore zone under breaking and nonbreaking conditions. *Journal of Geophysical Research: Oceans (1978–2012)*, 103(C6):12795–12805, 1998.

GuoHai Dong, Gang Wang, XiaoZhou Ma, and YuXiang Ma. Numerical study of transient nonlinear harbor resonance. *Science China Technological Sciences*, 53(2):558–565, 2010.

Young C Kim and Edward J Powers. Digital bispectral analysis and its applications to nonlinear wave interactions. *Plasma Science, IEEE Transactions on*, 7(2):120–131, 1979.

Thomas J Maccarone. The biphase explained: understanding the asymmetries in coupled fourier components of astronomical time series. *Monthly Notices of the Royal Astronomical Society*, page stt1546, 2013.

JOAN Alabart, AGUSTÍN Sanchez-Arcilla, and G Ph Van Vledder. Analysis of the performance of swash in harbour domains. In *Proceedings of the 3rd IAHR Europe congress, 1-10.(2014), Porto, Portugal*. IHAR, 2014.

Arnold Verruijt et al. Theory of groundwater flow. 1970.

Bart Mellink. Numerical and experimental research of wave interaction with a porous breakwater. 2012.

Swash team, 2015. User Manual SWASH version 2.00. URL http://swash.sourceforge.net/download/zip/swashuse.pdf.

EC Bowers. Low frequency waves in intermediate water depths. *Coastal Engineering Proceedings*, 1(23), 1992.

AJHM Reniers, AR Van Dongeren, JA Battjes, and EB Thornton. Linear modeling of infragravity waves during delilah. *Journal of Geophysical Research: Oceans (1978–2012)*, 107(C10):1–1, 2002.

AJHM Reniers, MJ Groenewegen, KC Ewans, S Masterton, GS Stelling, and J Meek. Estimation of infragravity waves at intermediate water depth. *Coastal Engineering*, 57(1):52–61, 2010.

DP Rijnsdorp. *Numerical modelling of infragravity waves in coastal regions*. PhD thesis, TU Delft, Delft University of Technology, 2011.

Rafael Guedes, Karin R Bryan, and Giovanni Coco. Observations of wave energy fluxes and swash motions on a low-sloping, dissipative beach. *Journal of Geophysical Research: Oceans*, 118(7):3651–3669, 2013.

TT Janssen, JA Battjes, and AR Van Dongeren. Long waves induced by short-wave groups over a sloping bottom. *Journal of Geophysical Research: Oceans (1978–2012)*, 108(C8), 2003.